BiOBr/MXene/gC$_3$N$_4$ Z-scheme heterostructure photocatalysts mediated by oxygen vacancies and MXene quantum dots for tetracycline degradation: Process, mechanism and toxicity analysis

Kexuan Gao [a], Li-an Hou [a,b], Xiaoqiang An [c], Doudou Huang [a], Yu Yang [a,*]

[a] State Key Laboratory of Water Environment Simulation, School of Environment, Beijing Normal University, Beijing 100875, China
[b] 96911 Unit, Beijing 100011, China
[c] Center for Water and Ecology, State Key Joint Laboratory of Environment Simulation and Pollution Control, School of Environment, Tsinghua University, Beijing 100084, China

ARTICLE INFO

ABSTRACT

The rapid recombination rate of photogenerated charges make the rational design of high-performance stable photocatalysts challenging. Herein, the features of heterojunctions, oxygen vacancies (OVs), and MXene quantum dots (MQDs) were simultaneously collected in CBM (gC$_3$N$_4$/BiOBr/MXene) using a simple solvothermal method for the first time. OVs promoted the chemisorption of O$_2$, MQDs not only accelerated electron transport but also promoted a photogenerated charge to selectively generate singlet oxygen, 99% of the tetracycline hydrochloride (TC-HCl) was degraded by CBM within 30 min under visible light irradiation. Thirteen intermediates and possible photocatalytic degradation pathways were proposed. It was discovered that CBM is nontoxic to the environment but can swiftly produce an excellent antibacterial effect when exposed to visible light irradiation. This research provides fresh insights into the effective removal of organic pollutants from water by combining cutting-edge defect engineering and quantum dot doping technology in photocatalytic heterojunctions.

1. Introduction

Tetracycline (TC), a common antibiotic, has been found in rivers and lakes all over the world as a result of widespread use and pharmaceutical wastewater discharge [1,2]. Physical adsorption could only simply adsorb tetracycline, while no substantial degradation or mineralization occur [3]. To reduce the environmental and ecological risks brought by TC, the use of green photocatalytic technology, which has been considered one of the most promising strategies [4], plays an important role in overcoming the defects of traditional wastewater treatment technology [5]. However, it is widely known that the greatest bottleneck that photocatalysts encounter is the rapid recombination rate of photogenerated charges and their wide band gaps [6,7].

Graphitic carbon nitride (gC$_3$N$_4$) has attracted tremendous attention owing to its recognized metal-free property, high stability, suitable energy bandgap, and unique surface properties [8]. gC$_3$N$_4$-based nanostructures are emerging as ideal candidates for a variety of energy and photocatalytic applications and are widely used for photocatalytic water reduction and oxidation, pollutant degradation, and CO$_2$ reduction [9].

Ao et al. prepared gC$_3$N$_4$ with the synergistic removal of antibiotics and Cr(VI) through simple thermal polymerization, and proposed that the electron-donating ability of contaminant molecule plays a decisive role in the photocatalysis removal efficiency [10]. However, the sluggish charge carrier migration and fast electron-hole recombination rate limit the photocatalytic activity [11]. To accelerate the separation of photogenerated charge carriers of gC$_3$N$_4$, diverse approaches, including heterojunction construction [12], defect creation, and metal/nonmetal doping, have been developed to make more efficient use of the advantages of gC$_3$N$_4$ and improve the conversion efficiency of solar energy [13,14]. Among them, the construction of heterojunctions is an effective and feasible strategy to improve catalytic performance, and the selection of semiconductors with suitable energy band structures is a critical step toward forming gC$_3$N$_4$-based heterostructures with improved performance.

Recently, several studies were conducted with the aim of enhancing photodegradation through the introduction of oxygen vacancies for the purpose of degrading antibiotics [15] and producing photocatalytic hydrogen [16]. It is widely known that OVs with plentiful localized

electrons occupying the O 2p orbital can significantly activate the oxygen-deficient surface as an electron-rich center, which could provide more oxygen adsorption sites, reduce the band gaps of semiconductors, promote the separation of electron-hole pairs, and improve the visible light response ability [17]. It has been demonstrated that abundant OVs are present below the conduction band of bismuth oxybromide (BiOBr) semiconductors. In addition, compared to their bulk counterparts, ultrathin 2D BiOBr materials more easily expose oxygen vacancies [18]. With its distinctive layer structure [19], chemical stability under visible light irradiation, and intrinsic flaws, the p-type BiOBr semiconductor is a promising option for heterojunction formation [20,21]. Importantly, due to their different energy band positions, gC_3N_4 and BiOBr are expected to form staggered Z-scheme heterostructures. Based on the layered structure characteristics and energy bands matched by gC_3N_4 and BiOBr, the constructed Z-scheme heterojunction showed enhanced photocatalytic performance [22,23]. The electrons are transferred from a semiconductor with corrected CB potential to another semiconductor with more negative VB potential, thus realizing effective separation of holes and electrons, and maintain high redox ability in the Z-scheme structure. Among the various heterojunction photocatalysts, the Z-scheme photocatalyst system formed by two semiconductors with different Fermi levels and suitable band structures exhibits a faster and more efficient separation of charges than the type-I and type-II heterojunctions [24]. Nevertheless, the transmission of photogenerated carriers is still the rate-limiting step of the photocatalytic process [25], and there is much room for improving the transport speed after photogenerated charge separation.

To better tackle this problem, the use of cocatalysts supported by photocatalysts is widely considered a robust strategy for promoting photogenerated electron and hole transport [26–28]. Precious metals have proven to be effective cocatalysts, but the prohibitive costs and shortages of natural reserves prevented their widespread usage. Two-dimensional (2D) transition metal carbides and nitrides (MXenes) [29], especially $Ti_3C_2T_x$, obtained by acid etching of Ti_3AlC_2 to remove the aluminum atomic layer while retaining its two-dimensional nature [30], with a high proportion of surface-exposed metal atoms, showed an extraordinary light-trapping efficiency and excellent electrical conductivity [31] and have emerged as a viable alternative for enhancing photocatalytic performance in environmental remediation [32,33]. In addition, the quantum dot forms usually have higher surface areas and forceful quantum confinement effects, which bring more meritorious properties [31,34]. The use of quantum dots with transverse dimensions less than 20 nm can avoid the common shielding effect of noble metal nanoparticles [35]. Schottky junctions formed by MXene quantum dots on the photocatalyst surface [16,26] could also enhance carrier mobility [36] and the interfacial coupling strength [29]. Previous studies have shown that $Ti_3C_2T_x$ exhibits excellent antibacterial properties under dark conditions at low concentrations when exposed to at least 4 h of continuous shaking [37,38], however, few studies have attempted to the introduce its quantum dot form into photocatalysts to study its antibacterial mechanism in photocatalytic processes. Based on the strong quantum confinement, excellent metallic conductivity, anisotropic carrier transport, large specific surface area, and other special properties of MQDs [39], innovatively introducing them into Z-scheme composite photocatalysts as fast electron transport channels reveal that photogenerated charge transport and antibacterial mechanisms in the process are important for the development of novel high-performance catalytic materials.

Inspired by the above concepts and strategies, our goal in this work is to design and develop an efficient Z-scheme heterojunction photocatalyst based on the synergistic action of MQDs and OVs to fully exploit solar energy and accelerate the degradation of tetracycline. MXene was introduced into the Z-scheme heterojunction of gC_3N_4 and BiOBr by using a simple ethylene glycol solvothermal method. MQDs with excellent electronic properties and a small size effect are expected to form a structural coupling process with OV-BiOBr to establish a

synergistic effect, inhibit electron reflux, increase charge separation efficiency and accelerate carrier transport. In particular, according to the identification of degradation intermediates, the degradation pathway of TC-HCl by h^+, $\bullet O_2^-$, $^1O_2$ and $\bullet OH$ was proposed. Moreover, the ecotoxicity of TC-HCl and its photodegradation intermediates were assessed and predicted via *Vibrio fischeri* and the Ecological Structure-Activity Relationships (ECOSAR) program, respectively. The antimicrobial properties of the material were evaluated by antibacterial experiments. The findings of this study are anticipated to provide novel mechanistic insights into the rapid separation and transport of photogenerated electrons and holes in photocatalysts.

2. Experimental

2.1. Chemicals

Melamine (99%), bismuth nitrate, potassium bromide, and L-histidine were obtained from Macklin Co., Ltd. Ti_3AlC_2 powders were purchased from Shandong Xiyan Co., Ltd. Ethylenediaminetetraacetic acid disodium salt (EDTA-2Na, 99%), p-benzoquinone (BQ, 99%), *tert*-butyl alcohol (TBA, $\geq$ 99%), 5,5-dimethyl-1-pyrroline-n-oxide (DMPO), and 2,2,6,6-tetramethylpiperidine (TEMP) were purchased from Shanghai Aladdin Biochemical Technology Co., Ltd. All chemicals were of analytical grade and used as received.

2.2. Synthesis of bulk gC_3N_4 and MXene

A crucible with a lid containing 5 g of melamine was calcinated in a muffle furnace using the following typical procedure: 520 °C for 4 h with a heating rate of 5 °C/min. After cooling to room temperature, the obtained yellow solid was ground into powder and collected for subsequent use.

MXene ($Ti_3C_2T_x$) was prepared by etching Ti_3AlC_2 powders. Typically, 2 g of lithium fluoride was dissolved in 40 ml HCl solution to produce hydrofluoric acid, and 1 g of Ti_3AlC_2 powder was slowly added with the aid of magnetic stirring. The suspension solution was placed in a 40 °C oil bath for 48 h. Then, the mixture was repeatedly washed with ultrapure water until the pH was greater than 6. The precipitate was collected and dissolved in 100 ml water and ultrasonicated for 2 h under a nitrogen atmosphere. After that, the mixture was centrifuged at 3500 rpm for 30 min. The centrifuge supernatant solution was vacuum freeze-dried to obtain solid MXene.

2.3. Synthesis of gC_3N_4/BiOBr/MXene composites

Protonated gC_3N_4 was obtained by treatment with 0.5 M hydrochloric acid, and surface charge modification via protonation of gC_3N_4 was used for electrostatic self-assembly to construct nanostructures. Two grams of gC_3N_4 was placed in 200 ml of HCl, dispersed uniformly by ultrasound for 2 h, stirred vigorously at room temperature for 6 h, washed with deionized water to neutral, dried and milled. Protonated gC_3N_4, $Bi(NO_3)_3 \cdot 5 H_2O$, and KBr were used as reactants without any surfactant, and the ethylene glycol solvothermal method at 180 °C for 24 h was utilized to synthesize the composites. The specific steps are as follows. First, 0.2 g protonated gC_3N_4 and MXene were added to 40 ml ethylene glycol followed by ultrasound treatment for 2 h to achieve even dispersion. $Bi(NO_3)_3 \cdot 5 H_2O$ and KBr were also dispersed in 10 ml DI water. Under vigorous stirring, the obtained uniform suspension of $Bi(NO_3)_3 \cdot 5 H_2O$ and KBr was dropped into the gC_3N_4 solution and stirred for 0.5 h, giving rise to a much more homogeneous and tight combination of materials. Subsequently, the mixture was transferred to a 100 ml Teflon-lined high-pressure autoclave. After cooling to room temperature, the precipitate was washed several times with water and ethanol. Finally, the composite was obtained by freeze-drying. By adjusting the addition of gC_3N_4 and Bi^{3+} in the precursor solution, gC_3N_4/BiOBr composites with theoretical mass ratios of 2:1, 1:1, 1:2,
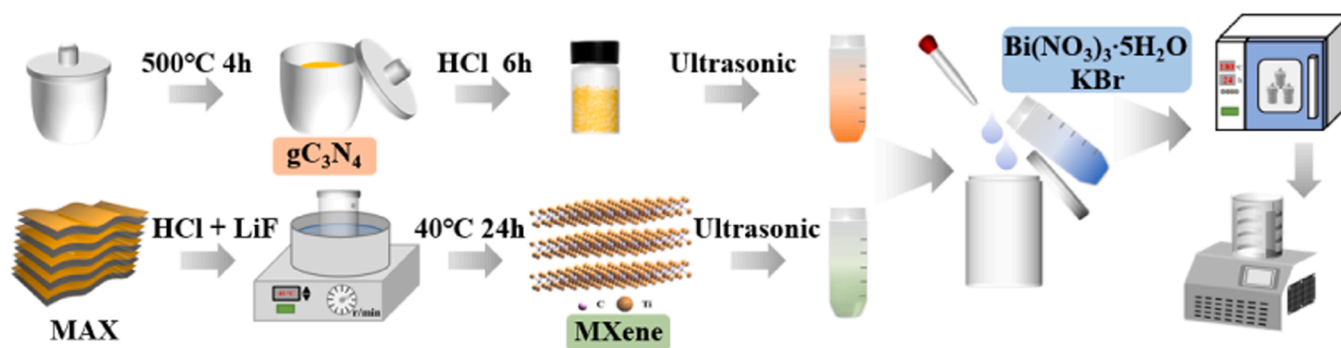
Fig. 1. Schematic illustration of the fabrication of photocatalytic composites.

1:5, and 1:8 were prepared, which were recorded as 2:1 CBM, 1:1 CBM, 1:2 CBM, 1:5 CBM, and 1:8 CBM, respectively. In addition, the preparation processes of pure BiOBr and 1:5 CB were similar (Fig. 1).

2.4. Characterization

Scanning electron microscopy (SEM) was used to analyze the surface morphology and microstructure of the catalyst. The elementary compositions of the samples were analyzed by EDS and elemental mapping. The surface functional groups and crystal structures of the synthesized composites were characterized by Fourier transform infrared spectroscopy (FT-IR, NEXUS 670) and powder X-ray diffraction (XRD, Rigaku Smartlab SE, Japan), respectively. X-ray photoelectron spectroscopy (XPS) measurements were performed on a Thermo Scientific ESCALAB 250Xi spectrometer equipped with Al Kα excitation. All binding energy values were calibrated for a C1s peak of 284.8 eV. Photoluminescence (PL) spectra were measured using a fluorescence spectrometer (Edinburgh Instruments, FLS1000). Electrochemical measurements, including transient photocurrent, electrochemical impedance spectroscopy (EIS), and Mott-Schottky analysis, were performed on a CHI 660 C Electrochemical Workstation (CHI Inc., USA).

2.5. Photocatalytic activity tests

2.5.1. Photocatalytic TC-HCl degradation

The activity of the as-prepared photocatalysts was assessed by TC-HCl degradation in a 50 ml flask reactor irradiated vertically by a 300 W Xenon lamp equipped with $400 - 780$ nm cut-off filters (Beijing PerfectLight, PLS-SXE300). The distance between the light source and the sample was 10 cm. Before the photoreaction, 10 mg of the photocatalyst was added to the TC-HCl solution (20 mg/L, 50 ml) and stirred for half an hour in darkness to achieve adsorption-desorption equilibrium. During the photocatalytic degradation reaction, 2 ml of dispersed solution was filtered with a 0.22 μm membrane at a given time interval. Then, the residual TC-HCl concentration in the solution was determined by high-performance liquid chromatography (HPLC, U-3000 Dionex USA) to evaluate the photodegradation effect. In addition, the pH of the solution was adjusted by HCl and NaOH to study the effect of the initial pH.

2.5.2. Active species trapping experiment

An active species trapping experiment was conducted to confirm the major active species in the photocatalytic systems. Radical scavengers such as benzoquinone (BQ), tert-butanol (TBA), ethylenediaminetetra-acetic acid disodium (EDTA-2Na), L-histidine, and silver nitrate (AgNO$_3$) were used to capture superoxide radicals ($\bullet$O$_2^-$), hydroxyl radicals ($\bullet$OH), holes (h$^+$), singlet oxygen (^{1}O$_2$), and electrons (e$^-$), respectively. Moreover, to further verify the production of reactive oxygen species (ROS) during the photocatalytic process, electron spin resonance (ESR, JES-FA100, JEOL Ltd., Tokyo, Japan) measurements

were conducted with 5,5-dimethyl-pyrroline N-oxide (DMPO) and tri-acetonamine (TEMP) as spin traps. Among them, the DMPO/water system and DMPO/methanol system were used to detect the existence of hydroxyl and superoxide radicals, respectively.

2.6. Identification of degradation products

Purification by solid-phase extraction column (SPE column) is necessary or even indispensable before the degradation products are analyzed by ultra-high-performance liquid chromatography combined with quadrupole time-of-flight mass spectrometry (UPLC-QTOF-MS). First, 5 ml methanol and 5 ml pure water were soaked for 10 min to activate the SPE column (C18, 500 mg, 6 ml), and 5 ml of sample flowed out naturally through the column. Then, inorganic ions were eliminated by adding 5 ml ultrapure water, and organic matter was eluted with 5–10 ml methanol. MS and MS/MS spectra were collected on a high-performance liquid chromatography-triple quadrupole mass spectrometer (LC-TOF-MS/MS, SCIEX 5600 +, SCIEX, USA) with a mobile phase composed of 0.1% aqueous formic acid (A) and acetonitrile (B) operating in cationic mode.

### 2.7. Toxicity assessment and ECOSAR evaluation

The toxicity assessment of the photocatalyst and photocatalytic behavior was divided into two parts. The first part was the ecological toxicity evaluation of the photocatalyst and the acute toxicity experiments of photocatalytic intermediates under visible light irradiation. *Pseudomonas aeruginosa,* as a typical gram-negative bacterium, has both intrinsic resistance and acquired resistance, which makes it very suitable for the ecotoxicity assessment of catalysts. Due to their distinct physiological traits, luminescent bacteria are frequently used in environmental monitoring as indicators to identify environmental toxins. The other part involved toxicity evaluation of the intermediates produced by photocatalysis tetracycline, including a luminescence inhibition rate experiment of photobacteria and acute toxicity (LC50) and chronic toxicity (ChV) prediction of the identified tetracycline and its intermediates through the ECOSAR (Ecological Structure Activity Relationships) prediction model. The method for using the ECOSAR prediction model developed by the U.S. Environmental Protection Agency was the same as that reported in previous literature [40,41]. Thus, the toxicity and photocatalytic behavior of the composites were determined through synthetic evaluation.

3. Results and discussion

3.1. Morphology and phase structures

AFM, TEM, and SEM scanning were performed to investigate the microstructures and morphologies of the prepared samples (Figs. 2 and S1). The materials were first dissolved in ethanol for 10 min before
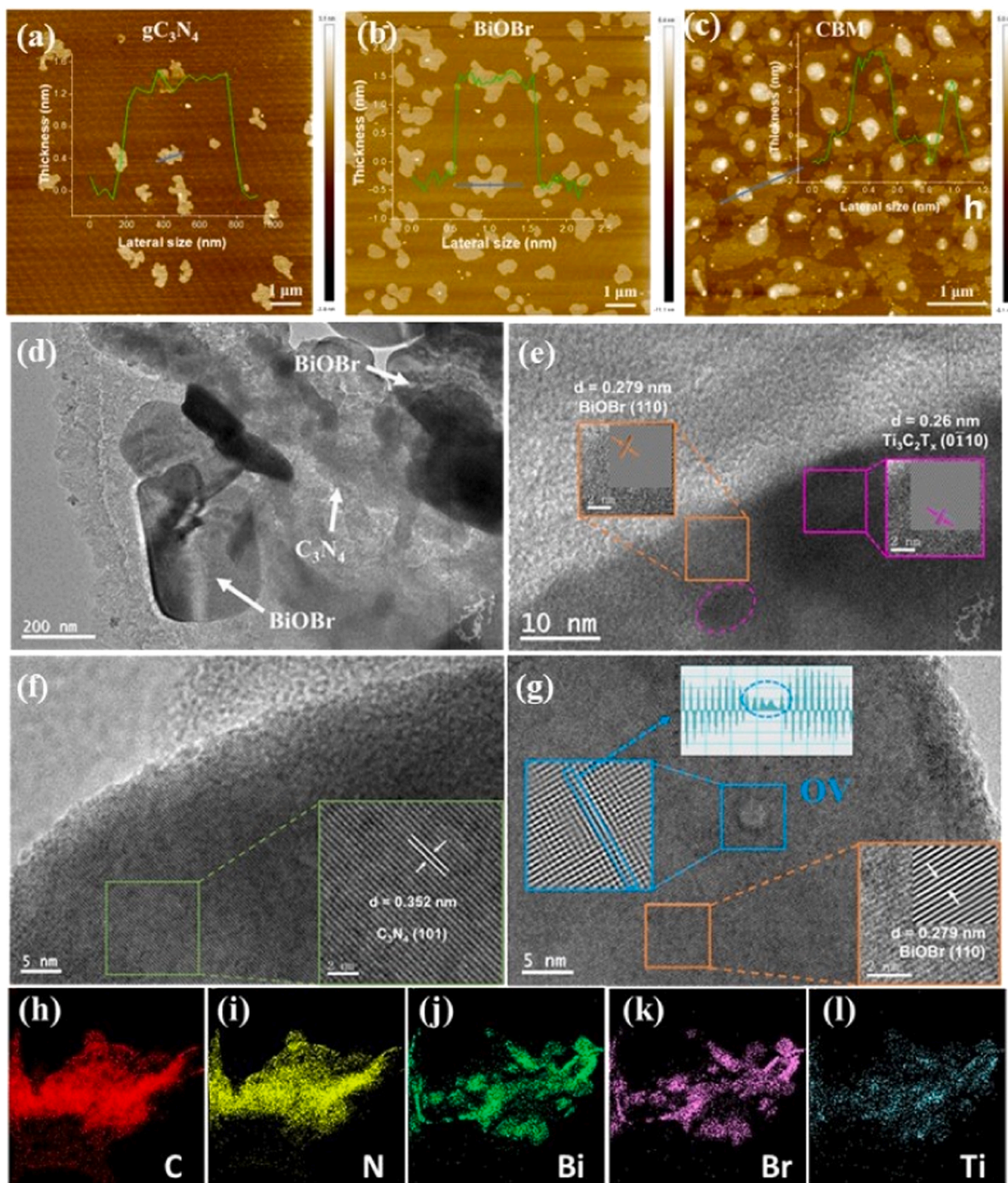
Fig. 2. AFM images of (a) gC₃N₄, (b) BiOBr, and (c) CBM; TEM (d), HRTEM (e-g) image and (h-l) element distribution mapping of CBM (the blue OV represents oxygen vacancies).

being dropped onto the mica sheet. Following the evaporation of ethanol, the AFM morphology of the materials was examined, as shown in Fig. 2(a-c). gC₃N₄ exhibited an irregular sheet structure with a single layer thickness of approximately 1.5 nm, while BiOBr showed an elliptical shape with a layer thickness of 2.0 nm. Interestingly, when the CBM heterojunction was formed, gC₃N₄ and BiOBr were tightly bonded,

forming a "fried egg" morphology, where the thinner gC₃N₄ is the "egg white" and BiOBr is the "egg yolk". Fig. S1(a-f) shows SEM images of each material. The pure gC₃N₄ was a massive structure composed of irregular lamellae, while BiOBr was an ordered nanosheet structure. The composite material exhibited a multilayer intercalation distribution, and there was no significant difference in the morphologies of different
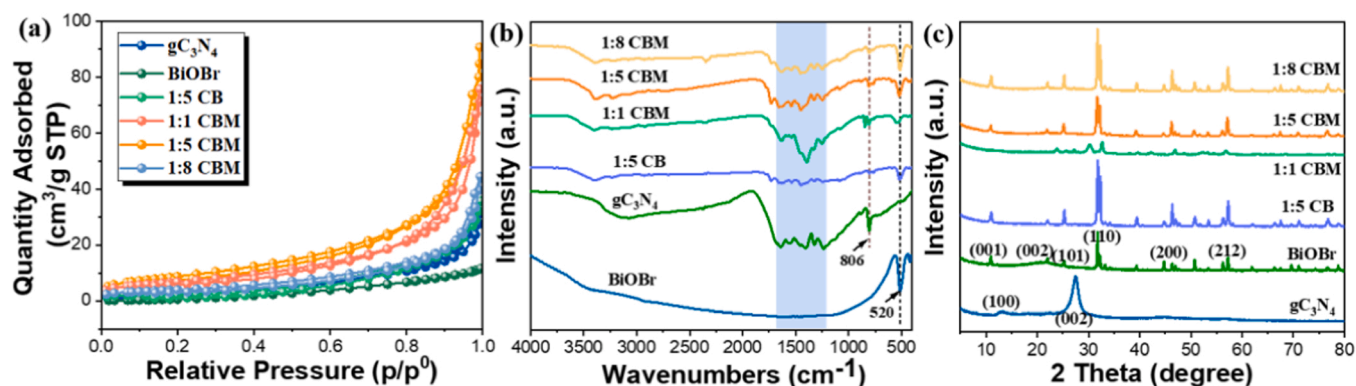
Fig. 3. (a) N$_2$ adsorption-desorption isotherms, (b) FTIR spectra, and (c) XRD patterns of the samples.

proportions of CBM. In addition, according to the TEM scanning (Fig. 2d) and the ratios of Bi and N elements (Fig. S1(g-i)) between lamellar and irregular wrinkled structures by spot scan, the main source of lamellar structure with clearly visible interfaces was BiOBr, while gC$_3$N$_4$ displayed an ultrathin wrinkled paper-fold sheet structure. The "fried egg"-like 2D/2D layered structure provided a good platform for the modification and loading of MXene. It is obvious that the ultrathin gC$_3$N$_4$ and the layered BiOBr were evenly dispersed, which could promote the openness of the materials [42,43], providing abundant reaction sites for organic small molecules and significantly improving the specific surface area of the material, thus generating vast contact interfaces and leading to a stronger improvement in the degradation ability [44].

The TEM and HRTEM images of 1:5 CBM, which are shown in Fig. 2g-i indicated that gC$_3$N$_4$, BiOBr, and MXene were well dispersed in the composite material. The EDS elemental mapping images of 1:5 CBM (Figs. 2 and S1) indicated that C, N, O, Bi, Br and Ti elements were homogeneously distributed throughout the particles and showed intimate contact, which ensured good electron transfer between the materials. The presence of Ti elements with atomic percentages less than 0.23% in the composites also serves as evidence for the successful incorporation of MXene. The HRTEM image (Fig. 2h-j) displays clear lattice fringes with interplanar spacings of 0.352 nm (green wireframe), 0.26 nm (purple wireframe), and 0.278 nm (orange wireframe), which can be indexed to the (101) plane of gC$_3$N$_4$, (0$\bar{1}$10) plane of Ti$_3$C$_2$T$_x$, and (110) plane of BiOBr, respectively [45]. The purple circle in Figs. 2h and S2 proves that the lateral size of MXene is approximately 10 nm, which means MXene was highly dispersed on gC$_3$N$_4$ and BiOBr in the form of MQDs (Fig. 2g). The intimate mutual contact between elements also effectively prevented individual MQDs from stacking or aggregating. It is worth noting that some oxygen vacancies (blue wireframe) appeared in the composite materials (Fig. 2i), which can be confirmed by the change in the spacing of adjacent lattice stripes marked with blue ellipses on the line profile of the inset of Fig. 2i. The coexistence of OVs and MQDs is a prerequisite for interfacial charge transfer.

The porosity and surface area of the catalyst are crucial factors affecting photocatalytic performance. Generally, the rich porous structures of photocatalysts are conducive to the exposure of catalytic active sites. The pore structure and properties of the catalyst were studied by the N$_2$ adsorption-desorption method (Fig. 3a). All samples presented type III isotherms with H3 hysteresis loops, indicating that the pores were mainly flat slit shapes. With the formation of heterojunctions, the specific surface area of the catalyst increased gradually, and Barrett—Joyner—Halenda (BJH) pore size analysis (Fig. S3) also showed an increase in the pore volume in the composites. The 1:5 CBM showed the highest specific surface area value, which proved that the 1:5 CBM could expose more photocatalytic active sites. The large pore volume was also conducive to the diffusion of pollutants and active radicals, thereby improving the photocatalytic degradation activity. FT-IR spectroscopy

was used to determine the structure and functional groups of the prepared photocatalyst (Fig. 3b). For the original gC$_3$N$_4$, the series of strong bands observed from 1235 to 1650 cm^{-1} corresponded to the typical stretching modes of CN heterocycles, and the adsorption peak at 806 cm^{-1} was attributed to the characteristic breathing mode of triazine units [2,46]. At the same time, the peak at 520 cm^{-1} of pure BiOBr corresponded to a symmetric stretching vibration from the Bi–O band [47]. The typical molecular structures of gC$_3$N$_4$ and BiOBr were still found in every composite, indicating that the synthetic samples retained the structure of the precursors. More importantly, the peak position of both gC$_3$N$_4$ and BiOBr has a slight redshift, especially in the 1:5 CBM, showing that a strong interaction between gC$_3$N$_4$, BiOBr, and MXene existed.

To further detect the chemical compositions, structures and crystal forms of the prepared samples, the XRD patterns of pure gC$_3$N$_4$, BiOBr, and the composites are shown in Fig. 3(c). gC$_3$N$_4$ exhibited two distinct diffraction peaks. The high-strength peak at 27.45° was related to the (002) crystal plane, which is attributed to the accumulation of aromatic segments, whereas the low-strength peak at 12.92° was associated with the (100) crystal plane, corresponding to the in-plane structure filling order [48]. The X-ray diffraction peaks of pure BiOBr at 10.900°, 21.928°, 32.220°, 46.208° and 57.116° corresponded to the (001), (002), (110), (200) and (212) crystal planes of tetragonal BiOBr, respectively (PDF #09–0393) [49]. The obtained (002) and (004) characteristic peaks (Fig. S4) of Ti$_3$C$_2$T$_x$ demonstrated successful etching of the precursor (Ti$_3$AlC$_2$).

All peaks of gC$_3$N$_4$ and BiOBr could be found in the patterns of the CB and CBM composites, which was consistent with the FT-IR results. BiOBr has a high crystallinity in the heterojunction, as evidenced by the sharp diffraction peak in the composites. Th fact that the characteristic peak of MXene was not detected in the composite is reasonable due to the low content. When compared to gC$_3$N$_4$ and BiOBr, the diffraction peak position of the composite showed no noticeable change, indicating that the photocatalyst prepared by the solvothermal method maintained its size and structure.

3.2. Photocatalytic performance and stability analysis

To evaluate the photocatalytic activity of the prepared materials for water purification, TC-HCl was photodegraded under visible light (400 nm $<\lambda<$ 780 nm). For pristine gC$_3$N$_4$ and BiOBr, only approximately 70% of TC-HCl was degraded after 80 min of visible irradiation. However, a remarkable enhancement in photocatalytic behavior was achieved with the formation of heterojunctions. The photocatalytic performance of CBM was superior to that of gC$_3$N$_4$, BiOBr and other binary composites, such as 1:5 CB. Most prominently, 1:5 CBM showed the rapid photodegradation of tetracycline under visible light irradiation, almost 100% of TC-HCl (20 mg/L) was degraded within 30 min, and the photocatalytic efficiency constant (k) was as high as
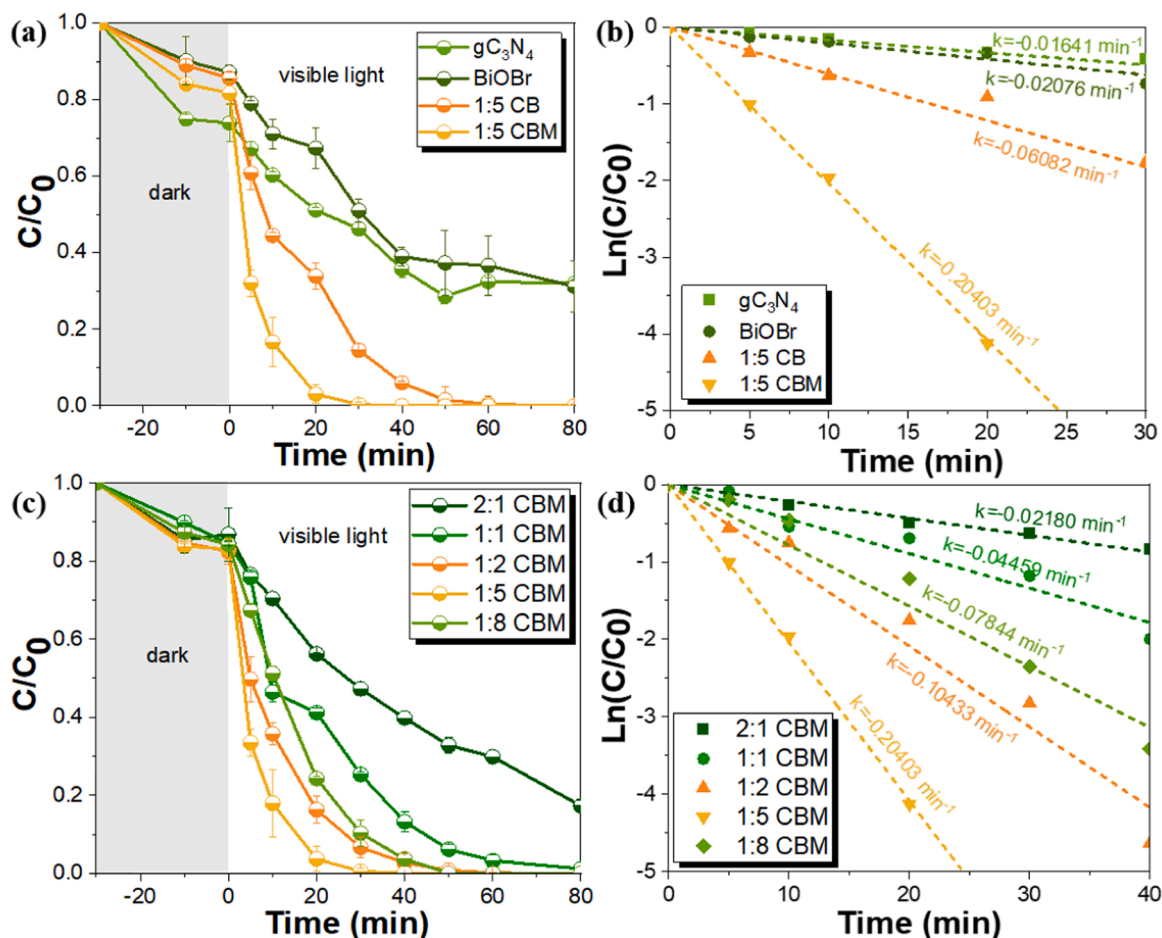
Fig. 4. Photocatalytic degradation kinetics (a,c) and the degradation rate constants (b,d) of TC-HCl by pure gC$_3$N$_4$, BiOBr and the various synthesized materials under visible light.

0.20403 min^{-1}. It was demonstrated that the strong interaction between gC$_3$N$_4$, BiOBr and MXene was crucial for the achievement of photodegradation behavior and that MQDs and OVs played a synergistic role in the improvement of the photocatalytic activity. Furthermore, to investigate the effect of the gC$_3$N$_4$ and BiOBr ratio on the photocatalytic degradation behavior, materials with gC$_3$N$_4$:BiOBr = 2:1, 1:1, 1:2, and 1:5 were prepared by adjusting the dosage of BiOBr. The photocatalytic degradation behavior is shown in Fig. 4c. With increasing BiOBr content, the photocatalytic degradation ability first increased and then decreased. The excessive deposition of BiOBr might affect the formation of the heterojunction and undermine the charge separation. This result is consistent with the change in the morphological characteristics of the composites observed by AFM and SEM. The change in MXene content may also have a certain influence on the performance of the photocatalyst, so the effect of MXene in the catalytic degradation process was explored by setting the following different proportions: 1%, 5%, 10%, 20%, 60% and 120% (accounting for the proportion of gC$_3$N$_4$). As shown in Fig. S5a, the catalytic rate is highest when the MXene content accounts for 5% of gC$_3$N$_4$, and the elimination efficiency of TC-HCl approaches 99% after 30 min. When the MXene content exceeds 20% of gC$_3$N$_4$, excess MXene hinders the photocatalytic degradation reaction. These phenomena can be explained by the fact that as the amount of MXene increases, more exposed charge-transfer sites are formed, but the quality and quantity of the effective heterogeneous interface encouraging charge transfer declines, which in turn reduces the photocatalytic performance. Considering the economy of the composite material under the premise of the full use of MXene, the amount of MXene added was set to 5% in this study.

It can be inferred that the introduction of appropriate amounts of BiOBr and MXene is conducive to achieving the best synergistic effect of the ternary heterojunction. The photodegradation behavior was fitted by pseudo first-order kinetics.

$$\ln(C_0/C_t) = Kt \qquad (1)$$

The kinetic degradation rate constant (K) of 1:5 CBM (0.204 min^{-1}) is 12 times higher than that of pure gC$_3$N$_4$ (0.016 min^{-1}).

As is well known, the initial pH of wastewater is a critical factor affecting the adsorption performance and surface chemical properties of photocatalysts. The pH dependence of adsorption and the photocatalytic behavior results are shown in Fig. S5b. Although the photocatalytic performance of the CBM photocatalyst fluctuated slightly with the change in the initial pH value, the heterojunction still exhibited considerable photocatalytic activity over a wide pH range (1−11). Besides, according to the analysis of zeta potential in different pH solution (Fig. S5c), 1:5 CBM shows a strongly negatively charged surface (< 20 mV) over a wide pH range. The zeta potential value decreased with the increase of pH, and the isoelectric point pH is 3.7. Tetracycline is an amphoteric molecule that is positively charged in solution when the pH is less than 3.3, neutral when the pH is between 3.3 and 7.7, and negatively charged when the pH is higher than 7.7 [50]. As a result, the ideal electrostatic adsorption environment only exists when the pH value is between 3.3 and 3.7, which is consistent with the relative optimal adsorption behavior in the dark when the initial pH is 3 in Fig. S5b. Overall, the change in initial pH did not affect the formation of the active substances, and the composite showed excellent photocatalytic performance, adaptability to pH conditions and good practical
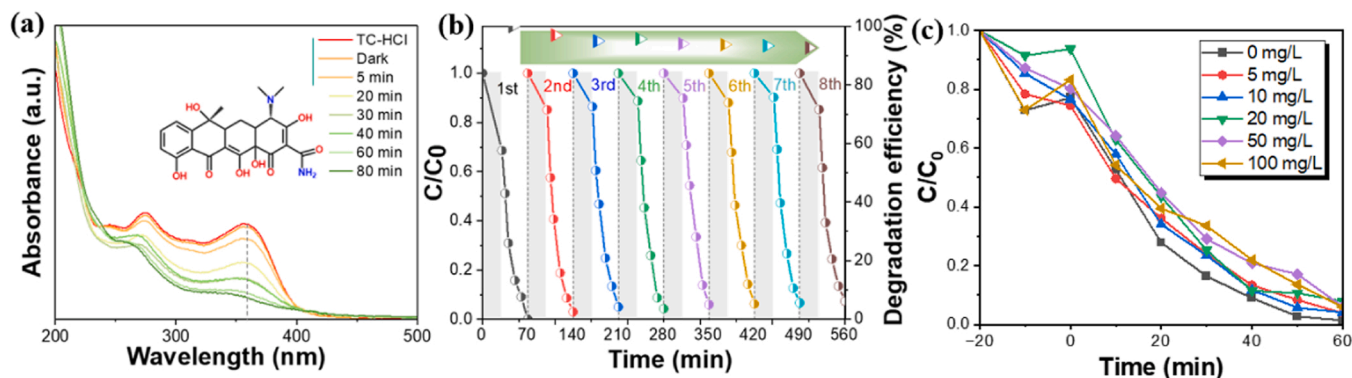
Fig. 5. (a) Representative UV–vis spectra changes of TC-HCl; (b) reusing CBM experiments for the degradation of TC-HCl over 8 cycles and (c) the effect of natural organic matter on the degradation of TC-HCl.
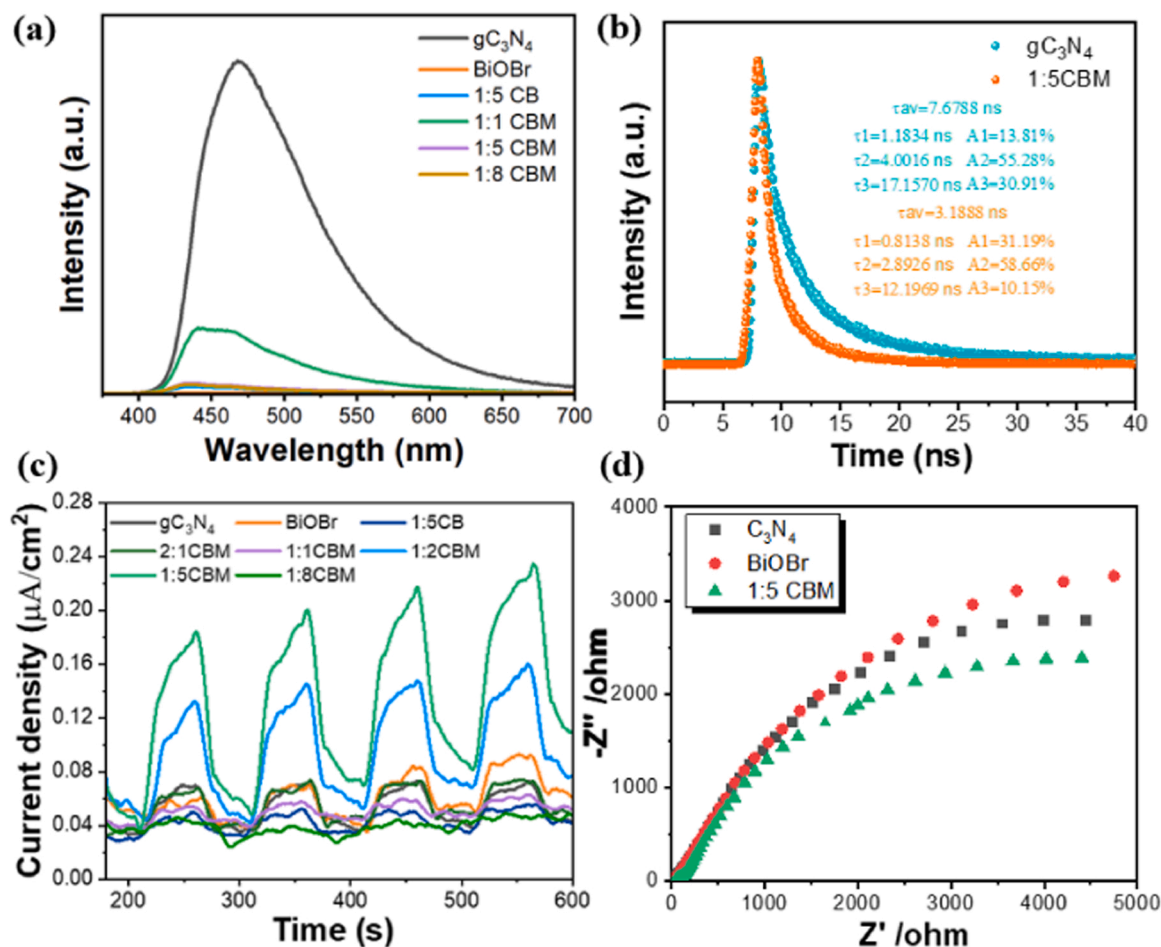

Fig. 6. The (a) steady-state and (b) transient photoluminescence (PL) spectra, (c) transient photocurrent response, and (d) EIS Nyquist plots of the samples.

potential.

Moreover, the degradation process of TC-HCl is shown in Fig. 5a. With increasing irradiation time, the peak intensity at 355 nm gradually decreases, indicating that TC-HCl and its intermediates have been degraded. To further explore the application feasibility, the recovery and recycling of CBM were studied for TC-HCl photodegradation carried out under identical conditions. The photocatalytic activity showed a slight decrease after eight cycles, and the degradation efficiency was still higher than 91% within 40 min. Humic acid, a typical model compound of natural organic matter, was used in this study to investigate the effect of NOM on the degradation of TC-HCl on CBM systems. Despite the HA

concentration reaching 100 mg/L, as seen in Fig. 5c, the efficiency degradation of CBM to TC-HCl remained high. The removal rate of TC-HCl only decreased from 99% to 94% as the HA concentration increased from 0 mg/L to 100 mg/L. This phenomenon may be due to the fact that high concentration of HA could act as a free radical scavenger to capture •OH in the reaction solution and compete for the active site [51,52], resulting in a slight reduction in the removal efficiency. To further evaluate the effectiveness of CBM in the photocatalytic process, the same concentrations of bisphenol A (BPA), carbamazepine (CBZ), and rhodamine B (RhB) were selected as model pollutants for photocatalytic degradation experiments. The removal efficiency of 1:5 CBM for BPA,
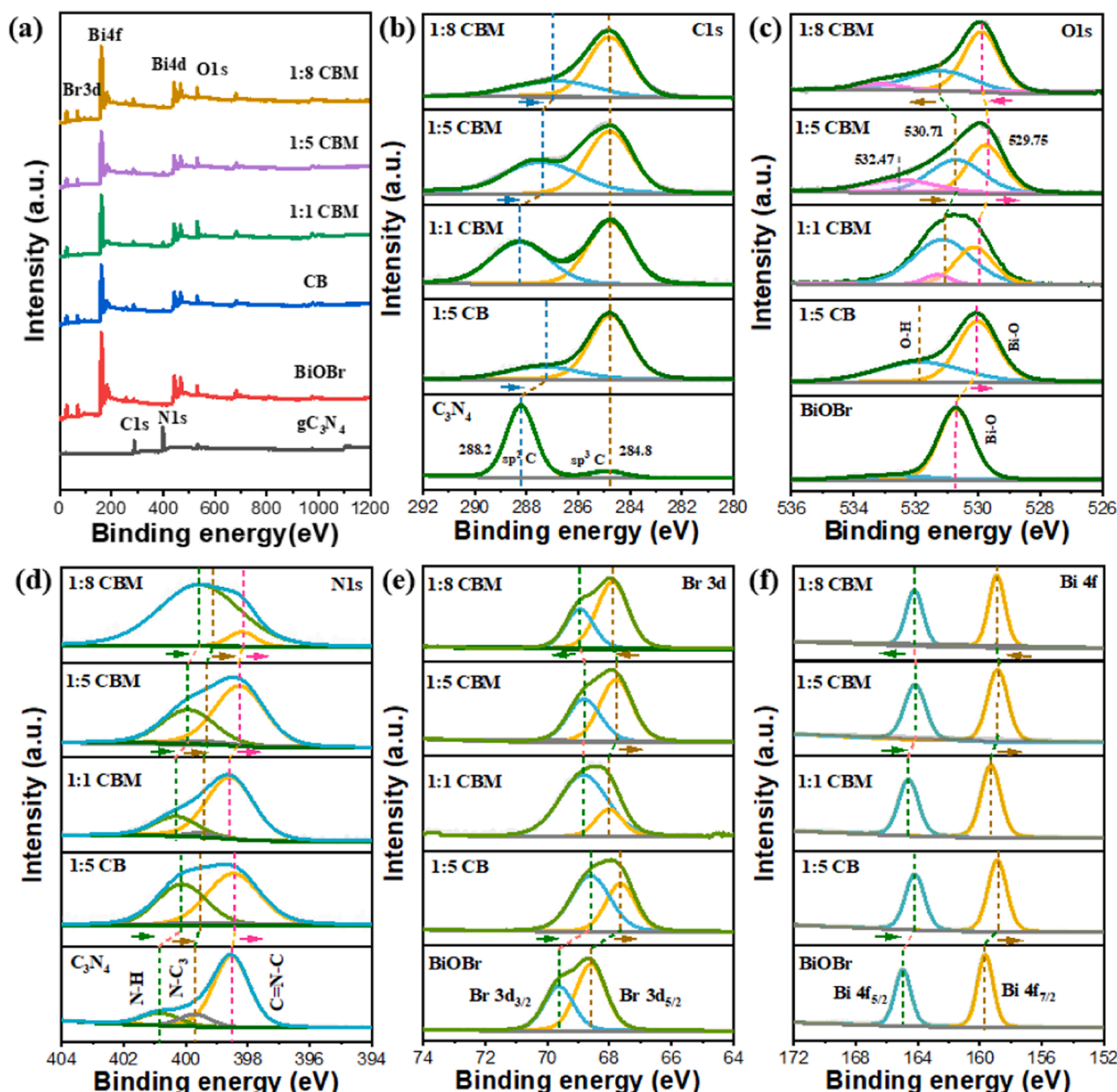
Fig. 7. XPS spectra of different composite materials: (a) full spectrum and their curve-fitting of (b) C 1s, (c) O 1s, (d) N 1s, (e) Br 3d and (f) Bi 4f.

RhB and CBZ reached 99%, 78% and 30% respectively (Fig. S5c), proving that CBM has the ability to degrade a variety of different dye and pharmaceuticals. As shown in Table S1, the photodegradation efficiency of CBM for TC-HCl was better than those of comparable photocatalysts previously reported. This fact signifies that CBM holds wastewater treatment application potential.

3.3. Proposed possible mechanism

3.3.1. Optical and electrical properties

To evaluate the separation efficiency of photogenerated carriers in semiconductor materials, the photoluminescence (PL) spectrum was studied by a fluorescence spectrometer (Edinburgh Instruments, FLS1000). The catalyst absorbs the energy in the light and then excites the excess energy, and the specific photoluminescence spectrum

produced by the recombination of excited electrons and valence band holes was called the PL spectrum. The larger the peak value in the spectrum is, the higher the recombination efficiency of electrons and holes.

The spectra of different composites were collected at 350 nm excitation wavelength at room temperature (Fig. 6a). gC$_3$N$_4$ showed the strongest emission peak at 470 nm. With the introduction of BiOBr and MXene into the heterojunction, the emission peak shows a blueshift, and the peak intensity presents a sharp decline, which is the lowest when the ratio of gC$_3$N$_4$ to BiOBr reaches 1:5, suggesting a more pronounced separation of photogenerated electrons and holes. The carrier life is significantly prolonged, which is one of the reasons for the improvement of the properties of the composites. Moreover, no PL signal was observed in pure BiOBr, indicating that no radiative recombination of photogenerated charges occurred in pure BiOBr at excitation wavelength of

350 nm [53,54]. A similar result was observed in the BiOBr-based heterojunction system by other groups [55]. In conclusion, the synthesized CBM heterojunctions were successful, and BiOBr provides a few electrons separately.

In order to explore the charge transfer dynamics, Fig. 6b showed the transient PL spectra of gC$_3$N$_4$ and 1:5 CBM, which provides information on the fluorescence lifetime of carriers. 1:5 CBM showed significantly reduced fluorescence lifetime ($\tau 1 = 0.8138$ ns, $\tau 3 = 12.1969$ ns, τav$=3.1888$ ns) compared to gC$_3$N$_4$ ($\tau 1 = 1.1834$ ns, $\tau 3 = 17.1570$ ns, τav$=7.6788$ ns). The decrease should be attributed to the presence of a more efficient nonradiative decay pathway [56,57] in 1:5 CBM, due to efficient interfacial charge transfer from BiOBr to gC$_3$N$_4$, result in the photo-induced charge carrier recombination can be effectively suppressed.

To further investigate the photoinduced charge separation and the migration efficiency and interfacial charge transfer resistance of the prepared photocatalysts, transient photocurrent experiments and electrochemical impedance spectroscopy (EIS) studies were carried out. As shown in Fig. 6c, all samples maintained excellent repeatability and stability after four intermittent irradiation cycles. The photocurrent intensity of the composite materials was much higher than that of pure gC$_3$N$_4$ and BiOBr. Among them, 1:5 CBM showed the highest photocurrent intensity compared with other proportions of CBM, which verified that the recombination of photogenerated carriers was greatly inhibited under this proportion. Similarly, the arc radius of the 1:5 CBM Nyquist diagram was the smallest compared with gC$_3$N$_4$ and BiOBr (Fig. 6d), indicating that the construction of heterojunctions improved the exciton dissociation and charge transfer property and made it easier to involve more electrons and holes in the photocatalytic degradation reaction [2], corresponding with the photodegradation activity results.

The transient photocurrent response, EIS and PL spectrum results demonstrated that the heterostructures fabricated through microstructural modulation, including the formation of heterostructures and the adjustment of the proportion of various components, facilitated separation and inhibited recombination of the photogenerated electron-hole pairs and could synergistically promote the photocatalytic degradation behavior.

3.3.2. Electronic structures of photocatalysts

Surface chemical information and the interaction between the elements for gC$_3$N$_4$, BiOBr and the composites were obtained through X-ray photoelectron spectroscopy (XPS). The XPS survey spectrum of the composite is shown in Fig. 7a. It has been validated that the composite possesses all the characteristic peaks of gC$_3$N$_4$ and BiOBr, including C 1 s, N1 s, O 1 s, Br 3d and Bi 4 f, without the existence of other impurity elements. According to the C 1 s XPS analysis of gC$_3$N$_4$, the binding energies at 284.8 eV (calibration peak) could be ascribed to the C-C coordination of the surface adventitious carbon, whereas that at 288.2 eV corresponds to sp^2-bonded carbon (N-C$=$N) [58,59]. The N 1 s peak of gC$_3$N$_4$ could be deconvoluted into three fitted peaks at 398.5, 399.7, and 400.8 eV, which were assigned to C$=$N-C, N-C$_3$, and N-H, respectively. Two main peaks of the O1s peak in BiOBr were observed at 530.7 eV and 532.8 eV, which were derived from Bi-O and O-H, respectively [54]. The Br 3d peak could be deconvoluted into two peaks at 68.6 eV and 69.6 eV, corresponding to the Br 3d$_{5/2}$ and Br 3d$_{3/2}$ characteristic peaks respectively. Bi 4 f was deconvoluted into Bi 4 f$_{7/2}$ and Bi 4 f$_{5/2}$ characteristic peaks at 159.6 eV and 164.95 eV, respectively.

Compared with the original gC$_3$N$_4$, the position of the sp^2 C characteristic peak (Fig. 7b) and the three characteristic peaks in N 1 s in 1:5 CB showed positive shifts with the addition of BiOBr, and the conversion trend of the binding energy value of Br 3d and Bi 4 f showed the same shift trend with the addition of gC$_3$N$_4$ relative to BiOBr (Fig. 7d). The binding energy shifts revealed that the formation of a heterojunction caused the movement of electrons, and there was a coupling interaction between gC$_3$N$_4$ and BiOBr. In comparison with 1:5 CB, the N 1 s

characteristic peak (Fig. 7d) of 1:5 CBM shows a slight positive shift, but the Br 3d characteristic peak (Fig. 7e) shows a slight negative shift, which proves that the addition of MXene promotes the movement of electrons from BiOBr to gC$_3$N$_4$. However, in each spectrum with different proportions of BiOBr (1:1, 1:5, 1:8), it can be found that with increasing BiOBr content, the characteristic peaks of sp2 C and N1s shift in the direction of the low binding energy, suggesting that the electron cloud density of gC$_3$N$_4$ changed after BiOBr modification, the electron cloud density increased on C and N, and electron transfer from BiOBr to gC$_3$N$_4$ was proven. Meanwhile, the change in BiOBr content caused the positive and then the negative movement of the O1s, Br 3d and Bi 4 f characteristic peaks, which also reflected the changing trend of the electron cloud density first increasing and then decreasing, and 1:5 CBM exhibits the highest electron cloud density, proving the highest hole and electron separation rate of BiOBr. For O1s, with increasing BiOBr content, the asymmetric oxygen signal in the 1:5 CBM could deconvolute into three different peaks at 529.75, 530.71, and 532.47 eV, indicating the presence of three different types of O atoms on the surface of the prepared catalyst. These O species were divided into (I) lattice oxygen (O1), (II) surface hydroxyl groups (O2) and (III) adsorbed oxygen (O3), in which the new adsorbed oxygen peak is attributed to the existence of oxygen vacancies [60].

As shown in Table S2, the proportion of oxygen species adsorbed on the surface of 1:5 CBM is approximately 20.78%, which is higher than that adsorbed on the surfaces of 1:1 CBM (3.88%) and 1:8 CBM (7.66%). In addition, it was found that the lattice oxygen ratio in 1:5 CBM (39.27%) was lower than that in 1:1 CBM (64.97%) and 1:8 CBM (56.80%). These results clearly indicated that more oxygen vacancies (OVs) are formed on the 1:5 CBM surface.

To clarify the source of oxygen vacancy generation, ESR analysis is shown in Fig. S6a. The pristine BiOBr possessed few vacancies, but the asymmetric ESR signal at g$=$ 2.003, which arose from the unpaired electrons trapped on surface OVs [61], could be clearly observed in the composites. The variation in signal intensity indicates the concentration variation of oxygen vacancies. When 1:5 CBM was compared to 1:1 CBM, the increase in BiOBr content resulted in an increase in oxygen vacancies, which indicated that BiOBr is the main contributor to oxygen vacancies. However, for 1:8 CBM, the excess BiOBr also leads to a decrease in the oxygen vacancy concentration. We assume the reason for this is that the layer stacking of BiOBr results in the inability to expose oxygen defects. Surprisingly, by comparing the changes in the 1:5 CB and 1:5 CBM signals, it can be seen that the addition of MQDs further encouraged the development of oxygen vacancies. The wide and strong characteristic peak of 1:5 CBM is considered to be the high OV concentration on the sample, which was conducive to adsorbing more O$_2$ to form more $\bullet$O$_2^-$ [62] and accompanied by the formation of singlet oxygen. In general, $\bullet$O$_2^-$, h$^+$, and ^{1}O$_2$ were always the main attacking species during the photocatalytic degradation of organic pollutants. This is consistent with the finding that 1:5 CBM emerged as the strongest oxidation capacity in the experimental results. The XPS and ESR results showed that the increase in oxygen vacancies leads to more adsorbed oxygen on the surface, which is conducive to the formation of reactive oxygen radicals and enhances photocatalytic activity [17,63]. At the same time, an internal electric field and intimate contact were formed at the interface between BiOBr, MQDs and gC$_3$N$_4$, and BiOBr and MQDs synergistically promoted charge separation and transfer in heterojunctions.

3.3.3. Free radical generation and migration pathways

UV$-$Vis diffuse reflectance spectra (DRS) of solid samples were collected by a UV$-$Vis-NIR spectrometer (SPECORD200 Varian, USA), which is shown in Fig. 9a. According to the cut-off wavelength of the sample absorption spectrum, the edge of the absorption band could be estimated. The band gap of the sample was calculated according to the following formula:
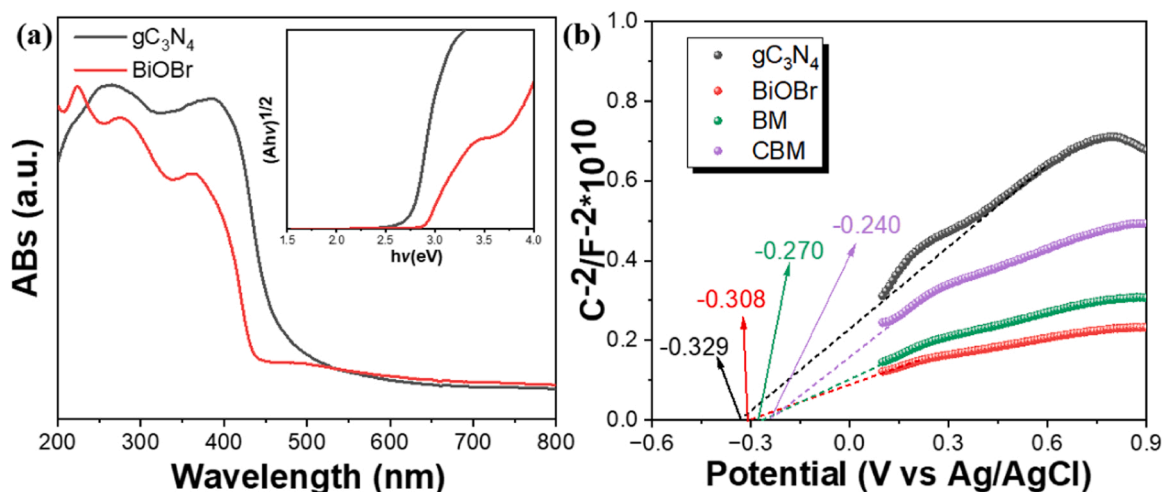
Fig. 8. (a) UV—Vis diffuse reflectance spectra (DRS), the plots of (Ahv)^2 vs. photon energy (hv) and (b) the Mott Schottky curve of gC$_3$N$_4$, BiOBr, BM (BiOBr+MXene) and CBM.
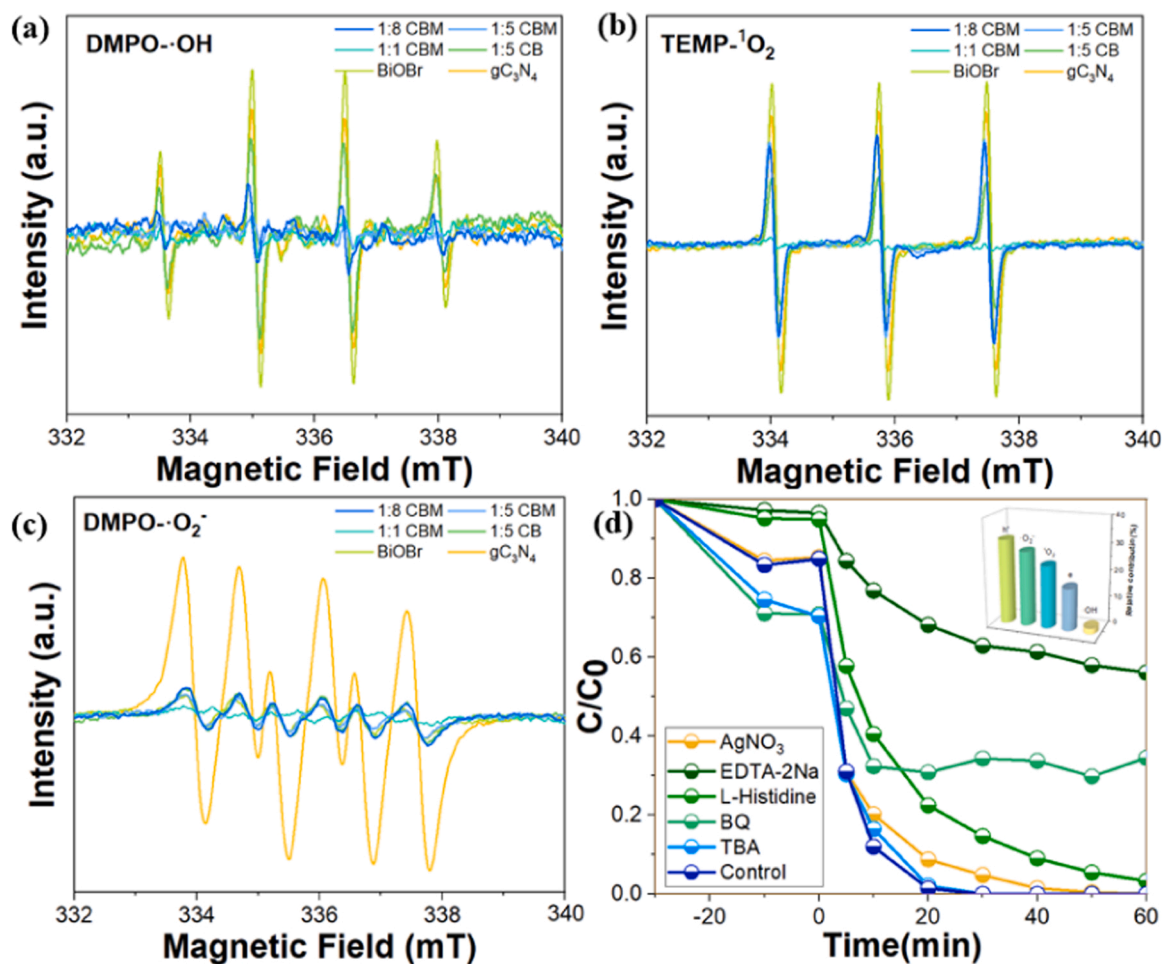

Fig. 9. The electron spin-trapping ESR spectra of samples with (a) DMPO dispersed in water for •OH, (b) TEMPO dispersed in water for ^{1}O$_2$ and (c)DMPO dispersed in methanol for •O$_2^-$.

$$\alpha h\upsilon = K\left(h\upsilon - E_g\right)^{m/2} \qquad (2)$$

where α is the absorption coefficient, $h\upsilon$ is the photon energy, K is the characteristic constant, E_g is the bandgap energy, m is determined by the type of electronic transition in the material, m= 1 represents the

direct bandgap semiconductors and m= 4 represents the indirect bandgap semiconductors.

As shown in Fig. 8a, the estimated Eg values for gC$_3$N$_4$ and BiOBr were 2.77 eV and 2.89 eV, respectively, which were consistent with those reported in previous studies [2]. To delve deeper into the
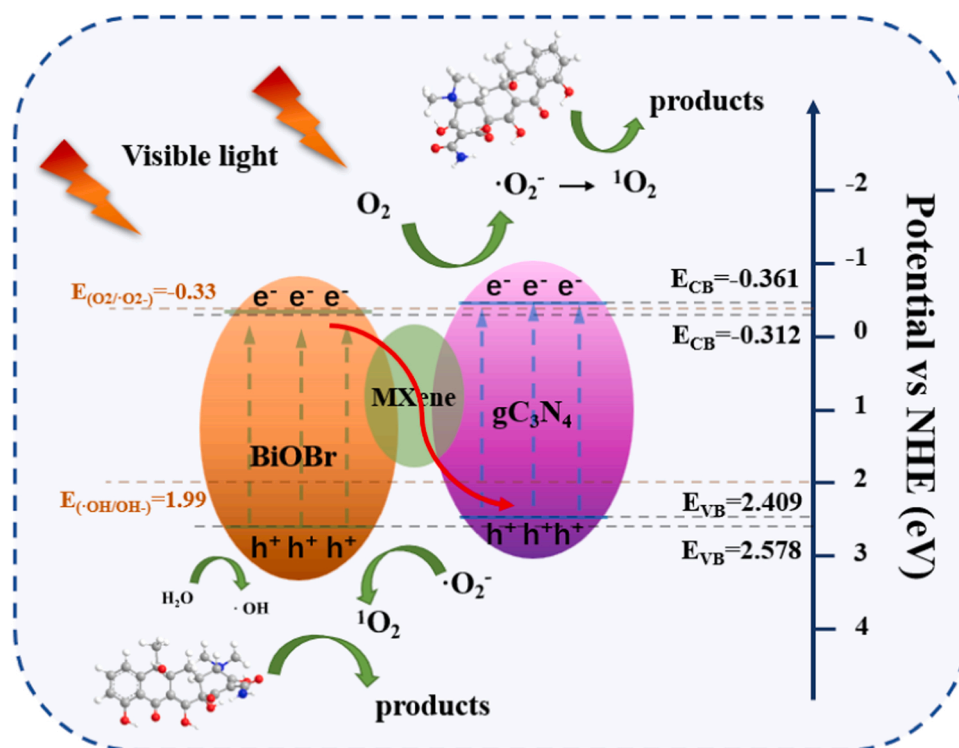
Fig. 10. Proposed mechanism of charge transfer and separation on the surface of CBM for TC-HCl degradation under visible light illumination.

photocatalytic mechanism of composite materials, XPS-VB was used to measure the valence band position (E_{VB}), and then the flat band potential (E_{fb}) was estimated by the Mott Schottky curve, as shown in Figs. S7 and 8(b). The valence band spectrum obtained from VB-XPS was calculated as follows: instrument work function - 4.44 + valence band spectrum tangent, and the work function of the instrument was 4.2. Therefore, the distances of the VB maximum and Fermi energy level of gC$_3$N$_4$ and BiOBr are 2.08 and 2.27 eV, respectively. The positive Mott Schottky slope indicated their n-type characteristics. The E_{fb} values of gC$_3$N$_4$ and BiOBr were − 0.329 and − 0.308 V vs. Ag/AgCl, respectively, which were identified by the x-intercept of the linear region. It is known that the Fermi level is approximate to the flat-band potential. The positions of E_{VB} for gC$_3$N$_4$ and BiOBr were thus determined to be 2.409 and 2.578 eV vs. NHE, respectively. The conduction band position (E_{CB}) was calculated according to $E_{CB} = E_{VB} − E_g$ (3), and finally, the band structure diagram was obtained (Fig. 10). From the structure of the photocatalyst, under visible light irradiation, both BiOBr and gC$_3$N$_4$ can be photoexcited and produce electron-hole pairs, and the photoinduced electrons migrate from VB to CB. Since the conduction band value of BiOBr was less negative than the redox potential of·O$_2$/O$_2$ (−0.33 eV) [64],·O$_2^-$ could not be obtained through this reaction, which was inconsistent with the results of the major active species obtained by ESR. Therefore, the traditional type II heterojunction does not conform to the structure of this composite. Photogenerated electrons on the BiOBr conduction band will rapidly transfer to MQDs and further transfer to the valence band of gC$_3$N$_4$ through the Z-scheme heterojunction. The photogenic electrons migrate to the surface of gC$_3$N$_4$ and react with the electron acceptor, while the holes remain on the surface of BiOBr and react with the electron donor molecules [65].

The Fermi levels for Ti$_3$C$_2$T$_x$ were estimated to be −0.05 V [66], which was between BiOBr and gC$_3$N$_4$, so MXene quantum dots could be used as an effective Z-scheme medium to promote electron transfer. Due to the characteristics of MXene as a transition metal, when BiOBr comes into contact with MQDs, photogenerated electrons on CB flow to the lower energy level MQDs until the matching Fermi energy levels reach equilibrium. The Mott Schottky measurement was performed to further

reveal the flat-band potential of BiOBr, BM (BiOBr+MXene) and CBM, as shown in Fig. 8b. The shift of the intercept towards positive values indicates an increase in the flatband potential, which suggests that the complex forms a Schottky barrier (Fig. S8a) [67,68]. The space charge layer was created on the BiOBr side, which bends the energy band upwards, and electrons captured by MQDs cannot flow back to the BiOBr CB, which boosts the separation of photoexcited electron-hole pairs. This can also be proven by comparing the photocurrent enhancement (Fig. 6b) and the open-circuit voltage increase (Fig. S8b) before and after MXene incorporation. Thus, photocarriers can be quickly transferred between gC$_3$N$_4$ and BiOBr via the Z-scheme with the help of MQDs due to the synergistic effect of the matched interacting band structure and the Schottky barrier. The MQDs act as a medium in the photocatalytic system to provide transmission channels for photogenerated electrons or holes.

To further elucidate the mechanism for the photocatalytic degradation of TC-HCl by the CBM system, electron spin-trapping (ESR, JES-FA100, JEOL Ltd., Tokyo, Japan) characterization and capture experiments were conducted to detect the generation of the ROS that was responsible for charge separation and the contribution of each active species in the photocatalytic process [2,69,70]. 5,5-dimethyl-1-pyrroline N-oxide (DMPO) and 2,2,6,6-tetramethylpiperidine (TEMP) were used as spin traps for ESR. As shown in Fig. S6(b-d), after 5 min of visible light irradiation, the formation of DMPO-•OH, DMPO-•O$_2^-$ and TEMP-^{1}O$_2$ could be clearly observed in the CBM system, and there were no ESR signals of ROS generated in the dark.

To further determine the charge transfer mechanism and determine the main active substances in the degradation process, the ESR spectra of materials with the same mass and concentration under illumination and the quenching experimental results of 1:5 CBM are shown in Fig. 9. Disodium ethylenediamine tetraacetate (EDTA-2Na), 1,4-benzoquinone (BQ), tert butanol (TBA), L-histidine and silver nitrate (AgNO$_3$) were used as scavengers of capture holes (h$^+$), superoxide radicals (•O$_2$), hydroxyl radicals (•OH), singlet oxygen (^{1}O$_2$) and electrons (e), respectively. The contribution rate (R) of free radicals was calculated using the following formula:
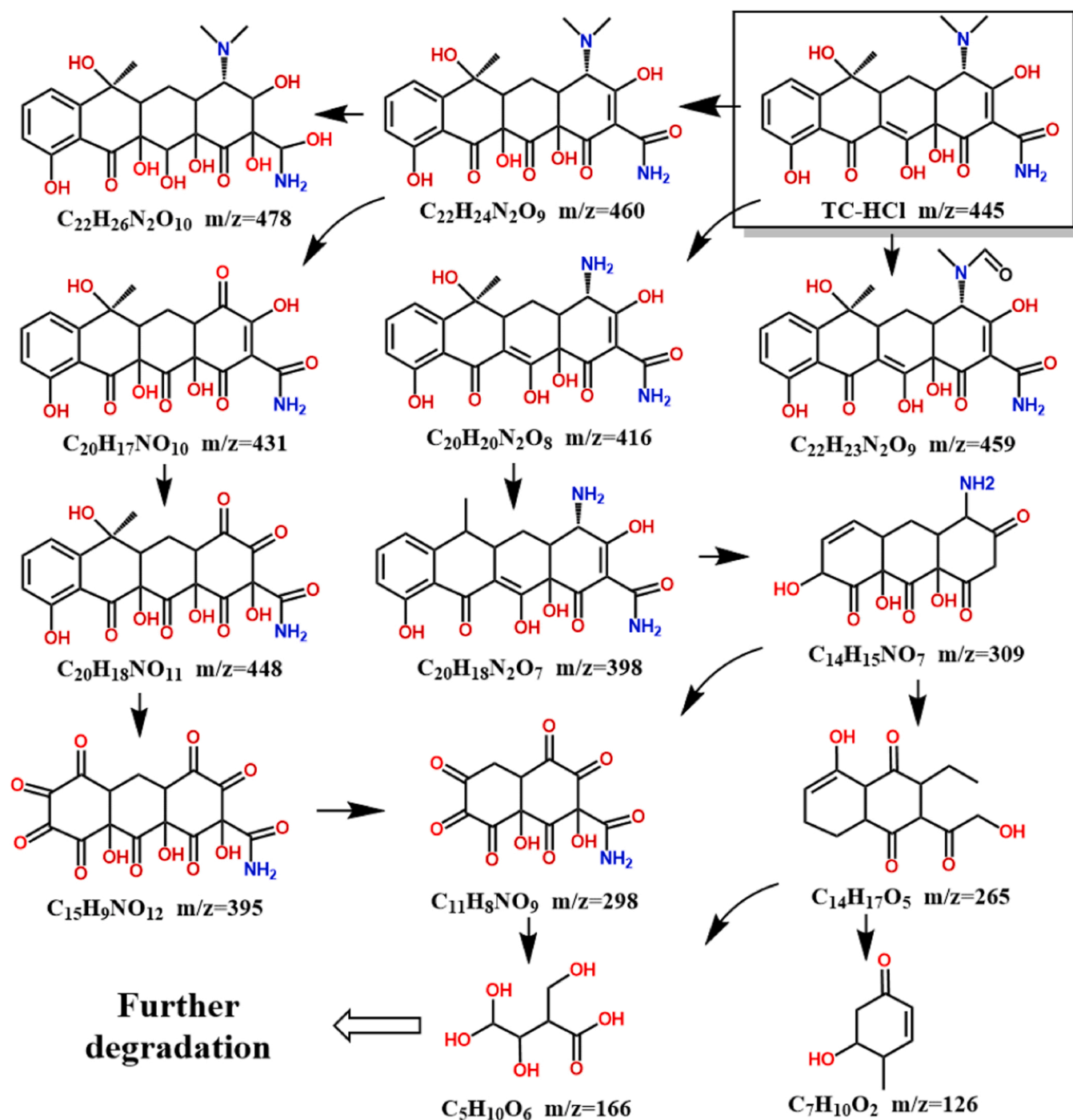
Fig. 11. Intermediates and possible photocatalytic degradation pathways of TC-HCl.

$$R(\%) = 1 - \frac{k_{scavenger}}{k_{blank}} \times 100\% \quad (3)$$

where $k_{scavenger}$ is the photodegradation rate of TC-HCl in the presence of scavenger and k_{blank} is the photodegradation rate of TC-HCl without scavenger.

First, both pure gC_3N_4 and BiOBr can be excited to generate electrons and holes under visible light, thereby generating hydroxyl radicals and reactive oxygen species. However, the heterojunction formation has different effects on the generation of free radicals. The holes lead to the generation of hydroxyl radicals in gC_3N_4 and BiOBr (Fig. 9a). However, the generation of hydroxyl radicals decreased significantly with the formation of heterojunctions and the addition of MXene. Compared with

1:5 CB, a significant decrease in hydroxyl radicals occurred in 1:5 CBM, while the amount of singlet oxygen showed a significant increase (Fig. 9b), proving that MQDs could induce the conversion of more vacancies into strong oxidizing reactive oxygen species, especially selectively generating more singlet oxygen and hindering the generation of hydroxyl radicals. Combined with the calculation results of the valence band conduction position, the conduction band value of gC_3N_4 was higher than the redox potential of·O_2^-/O_2, so many superoxide radicals were captured in the methanol system, while BiOBr produced only a small number of signals under illumination (Fig. 9c). The generation of superoxide radicals in the composite is slightly higher than that of BiOBr, which is mainly attributed to the contribution of the conduction band of gC_3N_4 after the formation of the Z-scheme heterojunction, but
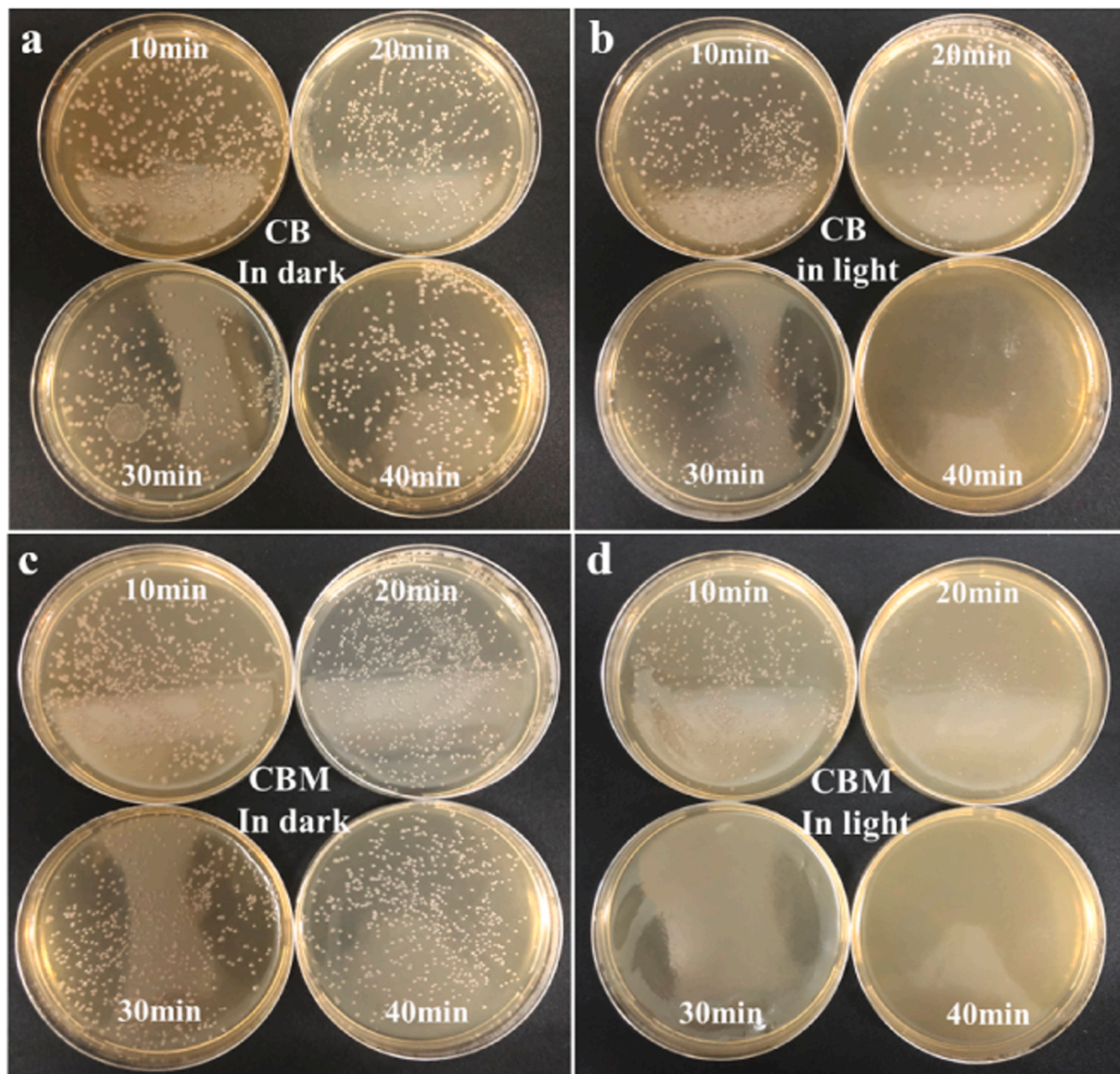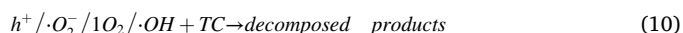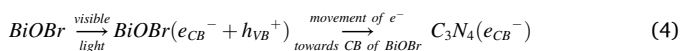
Fig. 12. (a, c) Ecological toxicity experiment in the dark and (b, d) photocatalytic bacteriostasis experiments of CB and CBM under visible light.

most of the superoxide radicals further react to generate singlet oxygen. Combined with the quenching reaction, when the superoxide radical and singlet oxygen were quenched, the oxidation effect decreased, while the quenching of hydroxyl radicals had little effect, further demonstrating that the oxidation effect in this heterojunction under light is mainly caused by reactive oxygen species. $^1O_2$ is directly involved in the degradation behavior of tetracycline.

CBM ternary composites produce hydroxyl radicals, superoxide radicals, holes and singlet oxygen nonradicals under visible light irradiation for photocatalytic degradation of TC-HCl. The degradation behavior was mainly driven by holes, singlet oxygen and superoxide radicals. Combined with ESR and radical quenching reactions, the overall electron transition and TC-HCl degradation reaction in CBM heterostructures were proposed as follows [65,71,72]:

$$BiOBr \xrightarrow[light]{visible} BiOBr(e_{CB}^- + h_{VB}^+) \xrightarrow[towards\ CB\ of\ BiOBr]{movement\ of\ e^-} C_3N_4(e_{CB}^-) \qquad (4)$$

$$C_3N_4(e_{CB})^- + O_2 \rightarrow \cdot O_2^- \qquad (5)$$

$$H_2O \Longleftrightarrow H^+ + \quad OH^- \qquad (6)$$

$$\cdot O_2^- + 2H^+ \rightarrow 2 \cdot OH \qquad (7)$$

$$BiOBr(h_{VB}^+) + OH^- \rightarrow \cdot OH \qquad (8)$$

$$h_{VB}^+ + \cdot O_2^- \rightarrow 1O_2 \qquad (9)$$

$$h^+ / \cdot O_2^- / 1O_2 / \cdot OH + TC \rightarrow decomposed \quad products \qquad (10)$$

According to the above results and energy band diagram, it can be concluded that there are two main factors contributing to the high photocatalytic activity of CBM. On the one hand, the large surface area and abundant OVs on the surface exposed more active sites for the degradation of reactant molecules, making the photocatalytic process
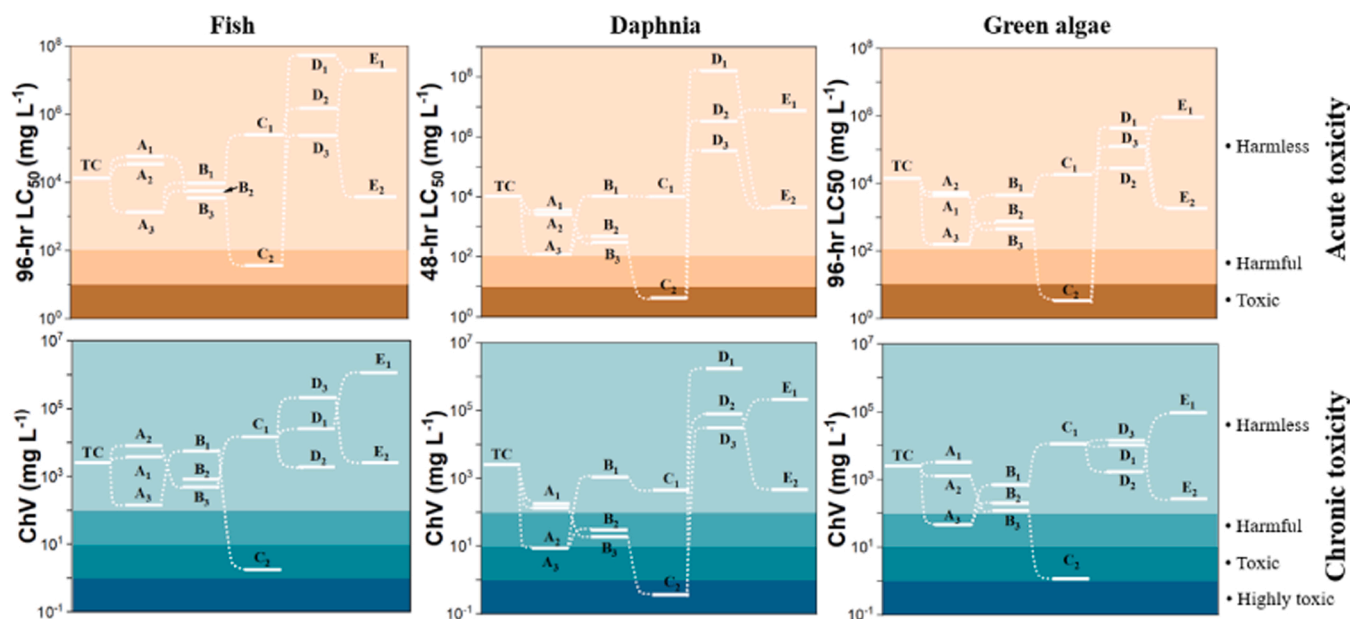
Fig. 13. Risk assessment of TC-HCl via ECOSAR in a CBM system.

more efficient. On the other hand, the highly conductive MQDs formed an effective charge collection and separation system for Z-scheme heterojunctions between gC_3N_4 and BiOBr, which not only formed a Schottky barrier to promote the separation of electrons but also induced the generation of more strongly oxidizing reactive oxygen species.

3.3.4. Intermediate product and the degradation pathway

As complete TC mineralization is hardly obtained, in this study, water samples were collected at different degradation times and the intermediates formed during TC-HCl photodegradation were characterized by UPLC-QTOF/MS (ESI positive mode) to further provide insight into its degradation pathway and mechanism. As shown in Figs. 11 and S9, S13, intermediates and possible photocatalytic degradation pathways of TC-HCl were proposed.

According to previous research, dimethylamino groups, amide groups and double bonds, as electron-donating groups and ionizable groups, are easily attacked by active free radicals [73,74], so the degradation process of TC-HCl mainly includes demethylation, deamination, deoxidation, hydroxylation, benzene ring-opening and deamidation. In this work, the hydroxylation, deamination and demethylation of TC-HCl led to a series of high molecular weight intermediates ($398 < m/z < 478$). With the increase in irradiation time, the degradation reaction proceeds further, and the benzene ring breaks off to form small tricyclic and bicyclic molecule products ($265 < m/z < 395$). Then, with the occurrence of benzene ring fracture and deamidation groups, TC-HCl is further effectively degraded into smaller products.

h^+, $\bullet O_2^-$, and $^1O_2$ and $\bullet OH$ generated by 1:5 CBM photoexcitation play the most direct roles in the destruction of the TC-HCl structure. h^+ and $\bullet O_2^-$ are mainly involved in the process of demethylation, deamination and deoxidation [75], while $^1O_2$ and relatively small amounts of $\bullet OH$ lead to hydroxylation [76], ring-opening and deamidation of TC-HCl [77].

3.4. Toxicology evaluation

Pseudomonas aeruginosa was used to evaluate the ecotoxicity of the photocatalyst under visible light (Fig. 12). Bacteria were cultivated over 24 h in lysogeny broth (LB) at 37 °C and allowed to grow until they reached the exponential phase. Then, the cells were centrifuged and washed with sterile PBS to remove macromolecules from the culture medium. In the absence of the catalyst, the bacterial solution was

exposed to visible light for 40 min as a blank control group, and bacterial solutions with different irradiation times were evenly inoculated on LB plate culture mediums. After incubation at 37 °C for 24 h, no significant change in the number of colonies occurred (Fig. S10 a), demonstrating that strong light did not significantly inhibit the growth of colonies. Under dark conditions, the catalysts were added to a PBS buffer containing suspended bacteria, and the growth trends of Pseudomonas aeruginosa samples treated with the CB and CBM photocatalysts were almost the same as that of the blank experiment, reflecting that the photocatalysts had no ecotoxicity effects on *Pseudomonas aeruginosa*. Intriguingly, bacteriostatic evaluation at different times under visible light irradiation showed different results. An obvious decrease in bacterial colonies can be observed on both CB and CBM with the progression of time. CB could attain 99% bacteriostatic efficiency at 40 min, while CBM could obtain an obvious bacteriostatic effect at 20 min, and 100% bacteriostatic efficiency was achieved at 30 min, which means CBM showed more marked antibacterial efficiency on *Pseudomonas aeruginosa* than CB, proving that after visible light irradiation, CBM could more quickly produce free radicals that could inhibit bacterial activity. This proved that the addition of MQDs could accelerate the separation and transmission of charges, which was consistent with the conclusion that the Schottky junction could inhibit electron reflux.

Bioluminescent bacteria (*Vibrio Fischeri*) were used to evaluate toxicity changes during TC-HCl degradation. Over time, the light intensity of luminescent bacteria fluctuated (Fig. S10 b). The inhibition rate did not change significantly under dark conditions, indicating that no degradation behavior had occurred. Bioluminescence was significantly inhibited in the first 5 min of visible light irradiation, indicating that some highly toxic intermediates were produced in the reaction process, while the luminescence inhibition rate showed a downwards trend at 40 min and 100 min, indicating that the intermediates were further degraded to produce substances with low toxicity levels.

In addition, ECOSAR software was used to analyse the quantitative structure-activity relationship (QSAR) of the intermediates, that is, their toxicity to fish, daphnia and algae, according to the structural formulas of the intermediates. The program could predict the acute and chronic toxicity of chemicals based on available data. The Global Harmonized Chemical Classification and Labeling System (GHS) indicates that fish, daphnia and algae can be regarded as substitutes for all aquatic organisms and that data for other species are comparable when tested. The

model results are listed in Fig. 13 and Table S3. Most TC-HCl degradation products were observed to be harmless (>100 mg/L) because they do not cause acute toxicity to fish, daphnia, or green algae. However, intermediate products with acute and chronic toxicity were also produced. Generally, the toxicity levels showed a trend of first increasing and then decreasing during the degradation process, with overall degradation in the direction of low toxicity, which was consistent with the test results of luminescent bacteria.

4. Conclusion

In conclusion, a Z-scheme heterojunction with tunable oxygen vacancies and rapid electron transport has been synthesized. The loading amount of BiOBr was related to the oxygen vacancy content, and MQDs can form Schottky junctions at the surface to inhibit electron reflux and accelerate photocarrier transfer. The synergistic effect of MQD, OVs and heterojunction formation of CBM resulted in fast charge transfer behavior and TC-HCl degradation efficiency. This improvement results from the increased number of exposed active sites, increased formation of adsorbed oxygen, forbidden recombination of electron-hole pairs and efficient production of reactive h^+, $\bullet O_2^-$ and $^1O_2$; 99% of the 20 mg/L TC-HCl was degraded by CBM within 30 min, which was 12 times the degradation efficiency of pure gC_3N_4. The *luminescence* inhibition rate of luminescent bacteria and ECOSAR prediction proved the degradation of TC-HCl in the direction of low toxicity. The photocatalysts had no ecotoxicity effects on *Pseudomonas aeruginosa*. The prepared photocatalyst has practical application potential.

CRediT authorship contribution statement

Kexuan Gao: Conceptualization, Methodology, Data curation, Writing – original draft, Writing – review & editing. **Li-an Hou**: Conceptualization, Supervision. **Yu Yang**: Supervision, Writing – review & editing, Project administration, Funding acquisition. **Xiaoqiang An**: Writing – review & editing. **Doudou Huang**: Methodology, Data curation.

Declaration of Competing Interest

The authors declare that they have no known competing financial interests or personal relationships that could have appeared to influence the work reported in this paper.

Data availability

I have shared the link to my data at the Attache file step.

Appendix A. Supplementary material

Supplementary data associated with this article can be found in the online version at doi:10.1016/j.apcatb.2022.122150.

References

[1] B. Xia, F. Deng, S. Zhang, L. Hua, X. Luo, M. Ao, Design and synthesis of robust Z-scheme ZnS-SnS₂ n-n heterojunctions for highly efficient degradation of pharmaceutical pollutants: performance, valence/conduction band offset photocatalytic mechanisms and toxicity evaluation, J. Hazard. Mater. 392 (2020), 122345, https://doi.org/10.1016/j.jhazmat.2020.122345.

[2] C. Liu, H. Dai, C. Tan, Q. Pan, F. Hu, X. Peng, Photo-Fenton degradation of tetracycline over Z-scheme Fe-g-C₃N₄/Bi₂WO₆ heterojunctions: mechanism insight, degradation pathways and DFT calculation, Appl. Catal. B Environ. 310 (2022), 121326, https://doi.org/10.1016/j.apcatb.2022.121326.

[3] M. Minale, A. Guadie, Y. Li, Y. Meng, X. Wang, J. Zhao, Enhanced removal of oxytetracycline antibiotics from water using manganese dioxide impregnated hydrogel composite: adsorption behavior and oxidative degradation pathways, Chemosphere 280 (2021), 130926, https://doi.org/10.1016/j.chemosphere.2021.130926.

[4] J. Wang, Q. Zhang, F. Deng, X. Luo, D.D. Dionysiou, Rapid toxicity elimination of organic pollutants by the photocatalysis of environment-friendly and magnetically recoverable step-scheme SnFe₂O₄/ZnFe₂O₄ nano-heterojunctions, Chem. Eng. J. 379 (2020), 122264, https://doi.org/10.1016/j.cej.2019.122264.

[5] J.C. Colmenares, R.S. Varma, P. Lisowski, Sustainable hybrid photocatalysts: titania immobilized on carbon materials derived from renewable and biodegradable resources, Green Chem. 18 (21) (2016) 5736–5750, https://doi.org/10.1039/C6GC02477G.

[6] Q. Xu, L. Zhang, B. Cheng, J. Fan, J. Yu, S-scheme heterojunction photocatalyst, Chem 6 (7) (2020) 1543–1559, https://doi.org/10.1016/j.chempr.2020.06.010.

[7] B. Wang, S.-Z. Yang, H. Chen, Q. Gao, Y.-X. Weng, W. Zhu, G. Liu, Y. Zhang, Y. Ye, H. Zhu, Revealing the role of oxygen vacancies in bimetallic PbBi₂Br atomic layers for boosting photocatalytic CO₂ conversion, Appl. Catal. B Environ. 277 (2020), 119170, https://doi.org/10.1016/j.apcatb.2020.119170.

[8] D. Huang, X. Sun, Y. Liu, H. Ji, W. Liu, C.-C. Wang, W. Ma, Z. Cai, A carbon-rich g-C₃N₄ with promoted charge separation for high efficient photocatalytic degradation of amoxicillin, Chin. Chem. Lett. 32 (9) (2021) 2787–2791, https://doi.org/10.1016/j.cclet.2021.01.012.

[9] J. Wen, J. Xie, X. Chen, X. Li, A review on g-C₃N₄-based photocatalysts, Appl. Surf. Sci. 391 (2017) 72–123, https://doi.org/10.1016/j.apsusc.2016.07.030.

[10] Q. Zhang, J. Chen, X. Gao, H. Che, P. Wang, Y. Ao, In-depth insight into the mechanism on photocatalytic synergistic removal of antibiotics and Cr (VI): the decisive effect of antibiotic molecular structure, Appl. Catal. B Environ. 313 (2022), 121443, https://doi.org/10.1016/j.apcatb.2022.121443.

[11] W. Huang, S. Ruan, M. Zhao, R. Xu, Z. Chen, G. Zhihong, H. Song, Visible-light-driven photocatalytic inactivation of Escherichia coli by 0D/2D CeO₂/g-C₃N₄ heterojunction: bactericidal performance and mechanism, J. Environ. Chem. Eng. 9 (6) (2021), 106759, https://doi.org/10.1016/j.jece.2021.106759.

[12] Z.-J. Bai, Y. Mao, B.-H. Wang, L. Chen, S. Tian, B. Hu, Y.-J. Li, C.-T. Au, S.-F. Yin, Tuning photocatalytic performance of Cs3Bi2Br9 perovskite by g-C3N4 for C (sp3)—H bond activation, Nano Res. (2022) 1–9, https://doi.org/10.1007/s12274-022-4835-z.

[13] H. Guo, H.-Y. Niu, C. Liang, C.-G. Niu, Y. Liu, N. Tang, Y. Yang, H.-Y. Liu, Y.-Y. Yang, W.-J. Wang, Few-layer graphitic carbon nitride nanosheet with controllable functionalization as an effective metal-free activator for peroxymonosulfate photocatalytic activation: Role of the energy band bending, Chem. Eng. J. 401 (2020), 126072, https://doi.org/10.1016/j.cej.2020.126072.

[14] Y. Yang, Z. Zeng, G. Zeng, D. Huang, R. Xiao, C. Zhang, C. Zhou, W. Xiong, W. Wang, M. Cheng, Ti₃C₂ Mxene/porous g-C₃N₄ interfacial Schottky junction for boosting spatial charge separation in photocatalytic H₂O₂ production, Appl. Catal. B Environ. 258 (2019), 117956, https://doi.org/10.1016/j.apcatb.2019.117956.

[15] F. Hasanvandian, M. Moradi, S.A. Samani, B. Kakavandi, S.R. Setayesh, M. Noorisepehr, Effective promotion of g–C₃N₄ photocatalytic performance via surface oxygen vacancy and coupling with bismuth-based semiconductors towards antibiotics degradation, Chemosphere 287 (2022), 132273, https://doi.org/10.1016/j.chemosphere.2021.132273.

[16] C. Cheng, J. Zhang, R. Zeng, F. Xing, C. Huang, Schottky barrier tuning via surface plasmon and vacancies for enhanced photocatalytic H₂ evolution in seawater, Appl. Catal. B Environ. 310 (2022), 121321, https://doi.org/10.1016/j.apcatb.2022.121321.

[17] W. Zhao, X. Wang, W. Wang, T. Han, H. Wang, H. Shi, Fabrication of oxygen vacancy-rich 3D/2D BiO₁₋ₓBr/BiOCl heterostructures towards efficient charge separation for enhanced photodegradation activity, Mater. Res. Bull. 143 (2021), 111448, https://doi.org/10.1016/j.materresbull.2021.111448.

[18] D. Xu, G. Li, Y. Dong, Q. Wang, J. Zhang, T. Yang, S. Pang, G. Zhang, L. Lv, Y. Xia, Photocatalytic O₂ activation enhancement and algae inactivation mechanism of BiO₂₋ₓ/Bi₃NbO₇ van der Waals heterojunction, Appl. Catal. B Environ. (2022), 121402, https://doi.org/10.1016/j.apcatb.2022.121402.

[19] Y. Shi, Y. Li, C. Mao, G. Zhan, Z. Yang, C. Ling, K. Wei, X. Liu, Z. Ai, L. Zhang, Manipulating excitonic effects in layered bismuth oxyhalides for photocatalysis, ACS ES&T Eng. (2022), https://doi.org/10.1021/acsestengg.1c00466.

[20] Q. Yan, X. Xie, Y. Liu, S. Wang, M. Zhang, Y. Chen, Y. Si, Constructing a new Z-scheme multi-heterojunction photocataslyts Ag/AgI/BiOI-Bi₂O₃ with enhanced photocatalytic activity, J. Hazard. Mater. 371 (2019) 304–315, https://doi.org/10.1016/j.jhazmat.2019.03.031.

[21] L. Meng, Y. Qu, L. Jing, Recent advances in BiOBr-based photocatalysts for environmental remediation, Chin. Chem. Lett. 32 (11) (2021) 3265–3276, https://doi.org/10.1016/j.cclet.2021.03.083.

[22] J. Lv, K. Dai, J. Zhang, Q. Liu, C. Liang, G. Zhu, Facile constructing novel 2D porous g-C₃N₄/BiOBr hybrid with enhanced visible-light-driven photocatalytic activity, Sep. Purif. Technol. 178 (2017) 6–17, https://doi.org/10.1016/j.seppur.2017.01.019.

[23] C. Liu, Q. Wu, M. Ji, H. Zhu, H. Hou, Q. Yang, C. Jiang, J. Wang, L. Tian, J. Chen, Constructing Z-scheme charge separation in 2D layered porous BiOBr/graphitic C₃N₄ nanosheets nanojunction with enhanced photocatalytic activity, J. Alloy. Compd. 723 (2017) 1121–1131, https://doi.org/10.1016/j.jallcom.2017.07.003.

[24] B. Xia, F. Deng, S. Zhang, L. Hua, X. Luo, M. Ao, Design and synthesis of robust Z-scheme ZnS-SnS₂ nn heterojunctions for highly efficient degradation of pharmaceutical pollutants: performance, valence/conduction band offset

photocatalytic mechanisms and toxicity evaluation, J. Hazard. Mater. 392 (2020), 122345, https://doi.org/10.1016/j.jhazmat.2020.122345.

[25] A. Meng, L. Zhang, B. Cheng, J. Yu, Dual cocatalysts in TiO_2 photocatalysis, Adv. Mater. 31 (30) (2019), 1807660, https://doi.org/10.1002/adma.201807660.

[26] V.Q. Hieu, T.C. Lam, A. Khan, T.-T.T. Vo, T.-Q. Nguyen, V.D. Doan, V.A. Tran, $TiO_2/Ti_3C_2/g-C_3N_4$ ternary heterojunction for photocatalytic hydrogen evolution, Chemosphere 285 (2021), 131429, https://doi.org/10.1016/j.chemosphere.2021.131429.

[27] Y. Jia, Z. Wang, X.-Q. Qiao, L. Huang, S. Gan, D. Hou, J. Zhao, C. Sun, D.-S. Li, A synergistic effect between S-scheme heterojunction and Noble-metal free cocatalyst to promote the hydrogen evolution of $ZnO/CdS/MoS_2$ photocatalyst, Chem. Eng. J. 424 (2021), 130368, https://doi.org/10.1016/j.cej.2021.130368.

[28] L. Wang, Y. Li, C. Wu, X. Li, G. Shao, P. Zhang, Tracking charge transfer pathways in $SrTiO_3/CoP/Mo_2C$ nanofibers for enhanced photocatalytic solar fuel production, Chin. J. Catal. 43 (2) (2022) 507–518, https://doi.org/10.1016/S1872-2067(21)63898-6.

[29] R. Xiao, C. Zhao, Z. Zou, Z. Chen, L. Tian, H. Xu, H. Tang, Q. Liu, Z. Lin, X. Yang, In situ fabrication of 1D CdS nanorod/2D Ti_3C_2 MXene nanosheet Schottky heterojunction toward enhanced photocatalytic hydrogen evolution, Appl. Catal. B Environ. 268 (2020), 118382, https://doi.org/10.1016/j.apcatb.2019.118382.

[30] C. Wei, Y. Tao, Y. An, Y. Tian, Y. Zhang, J. Feng, Y. Qian, Recent advances of emerging 2D MXene for stable and dendrite-free metal anodes, Adv. Funct. Mater. 30 (45) (2020), 2004613, https://doi.org/10.1002/adfm.202004613.

[31] F. He, B. Zhu, B. Cheng, J. Yu, W. Ho, W. Macyk, 2D/2D/0D $TiO_2/C_3N_4/Ti_3C_2$ MXene composite S-scheme photocatalyst with enhanced CO_2 reduction activity, Appl. Catal. B Environ. 272 (2020), 119006, https://doi.org/10.1016/j.apcatb.2020.119006.

[32] K. Zhang, D. Li, H. Cao, Q. Zhu, C. Trapalis, P. Zhu, X. Gao, C. Wang, Insights into different dimensional MXenes for photocatalysis, Chem. Eng. J. 424 (2021), 130340, https://doi.org/10.1016/j.cej.2021.130340.

[33] P. Zhang, Y. Li, Y. Zhang, R. Hou, X. Zhang, C. Xue, S. Wang, B. Zhu, N. Li, G. Shao, Photogenerated electron transfer process in heterojunctions: in situ irradiation XPS, Small Methods 4 (9) (2020), 2000214, https://doi.org/10.1002/smtd.202000214.

[34] B. Shao, Z. Liu, G. Zeng, H. Wang, Q. Liang, Q. He, M. Cheng, C. Zhou, L. Jiang, B. Song, Two-dimensional transition metal carbide and nitride (MXene) derived quantum dots (QDs): synthesis, properties, applications and prospects, J. Mater. Chem. A 8 (16) (2020) 7508–7535, https://doi.org/10.1039/D0TA01552K.

[35] K. Li, S. Zhang, Y. Li, J. Fan, K. Lv, MXenes as noble-metal-alternative co-catalysts in photocatalysis, Chin. J. Catal. 42 (1) (2021) 3–14, https://doi.org/10.1016/S1872-2067(20)63630-0.

[36] M. Ding, R. Xiao, C. Zhao, D. Bukhvalov, Z. Chen, H. Xu, H. Tang, J. Xu, X. Yang, Evidencing interfacial charge transfer in 2D CdS/2D MXene Schottky heterojunctions toward high-efficiency photocatalytic hydrogen production, Sol. RRL 5 (2) (2021), 2000414, https://doi.org/10.1002/solr.202000414.

[37] K. Rasool, M. Helal, A. Ali, C.E. Ren, Y. Gogotsi, K.A. Mahmoud, Antibacterial activity of $Ti_3C_2T_x$ MXene, ACS Nano 10 (3) (2016) 3674–3684, https://doi.org/10.1021/acsnano.6b00181.

[38] A. Arabi Shamsabadi, M. Sharifian Gh, B. Anasori, M. Soroush, Antimicrobial mode-of-action of colloidal $Ti_3C_2T_x$ MXene nanosheets, ACS Sustain. Chem. Eng. 6 (12) (2018) 16586–16596, https://doi.org/10.1021/acssuschemeng.8b03823.

[39] G. Ramalingam, P. Kathirgamanathan, G. Ravi, T. Elangovan, N. Manivannan, K. Kasinathan, Quantum confinement effect of 2D nanomaterials, Quantum Dots-Fundamental and Applications, IntechOpen, 2020.

[40] Y. Yang, X. Lu, J. Jiang, J. Ma, G. Liu, Y. Cao, W. Liu, J. Li, S. Pang, X. Kong, Degradation of sulfamethoxazole by UV, UV/H_2O_2 and UV/persulfate (PDS): formation of oxidation products and effect of bicarbonate, Water Res. 118 (2017) 196–207, https://doi.org/10.1016/j.watres.2017.03.054.

[41] W. Yang, Y. Wang, Enhanced electron and mass transfer flow-through cell with C_3N_4-MoS_2 supported on three-dimensional graphene photoanode for the removal of antibiotic and antibacterial potencies in ampicillin wastewater, Appl. Catal. B Environ. 282 (2021), 119574, https://doi.org/10.1016/j.apcatb.2020.119574.

[42] J. Liu, G. Wang, B. Li, X. Ma, Y. Hu, H. Cheng, A high-efficiency mediator-free Z-scheme Bi_2MoO_6/AgI heterojunction with enhanced photocatalytic performance, Sci. Total Environ. 784 (2021), 147227, https://doi.org/10.1016/j.scitotenv.2021.147227.

[43] B. He, Y. Du, Y. Feng, M. Du, J. Wang, J. Qu, Y. Liu, N. Jiang, J. Wang, X. Sun, Fabrication of novel ternary direct Z-scheme$^+$ isotype heterojunction photocatalyst $g-C_3N_4/g-C_3N_4/BiOBr$ with enhanced photocatalytic performance, Appl. Surf. Sci. 506 (2020), 145031, https://doi.org/10.1016/j.apsusc.2019.145031.

[44] Q. Yan, T. Zhang, Y. Fu, Y. Zeng, C. Xu, P. Wang, X. Zhou, Nickel-doping accelerated charge separation in flower ball-like $Bi_4O_5I_2$ for efficient visible-light photocatalytic performance, Appl. Surf. Sci. 540 (2021), 148310, https://doi.org/10.1016/j.apsusc.2020.148310.

[45] J. Li, Z. Li, X. Liu, C. Li, Y. Zheng, K.W.K. Yeung, Z. Cui, Y. Liang, S. Zhu, W. Hu, Interfacial engineering of $Bi_2S_3/Ti_3C_2T_x$ MXene based on work function for rapid photo-excited bacteria-killing, Nat. Commun. 12 (1) (2021) 1–10, https://doi.org/10.1038/s41467-021-21435-6.

[46] L. Huang, J. Liu, P. Li, Y. Li, C. Wang, S. Shu, Y. Song, CQDs modulating Z-scheme $g-C_3N_4/BiOBr$ heterostructure for photocatalytic removing RhB, BPA and TC and E. coli by LED light, J. Alloy. Compd. 895 (2022), 162637, https://doi.org/10.1016/j.jallcom.2021.162637.

[47] M. Li, Q. Lu, M. Liu, P. Yin, C. Wu, H. Li, Y. Zhang, S. Yao, Photoinduced charge separation via the double-electron transfer mechanism in nitrogen vacancies $g-C_3N_5/BiOBr$ for the photoelectrochemical nitrogen reduction, ACS Appl. Mater.

Interfaces 12 (34) (2020) 38266–38274, https://doi.org/10.1021/acsami.0c11894.

[48] Y.-P. Zhu, M. Li, Y.-L. Liu, T.-Z. Ren, Z.-Y. Yuan, Carbon-doped ZnO hybridized homogeneously with graphitic carbon nitride nanocomposites for photocatalysis, J. Phys. Chem. C 118 (20) (2014) 10963–10971, https://doi.org/10.1021/jp502677h.

[49] M. Li, C. Song, Y. Wu, M. Wang, Z. Pan, Y. Sun, L. Meng, S. Han, L. Xu, L. Gan, Novel Z-scheme visible-light photocatalyst based on $CoFe_2O_4/BiOBr/Graphene$ composites for organic dye degradation and Cr (VI) reduction, Appl. Surf. Sci. 478 (2019) 744–753, https://doi.org/10.1016/j.apsusc.2019.02.017.

[50] H. Huang, Y. Chen, X. Zheng, T. Su, R. Wan, S. Yang, Distribution of tetracycline resistance genes in anaerobic treatment of waste sludge: the role of pH in regulating tetracycline resistant bacteria and horizontal gene transfer, Bioresour. Technol. 218 (2016) 1284–1289, https://doi.org/10.1016/j.biortech.2016.07.097.

[51] X. Li, T. Chen, Y. Qiu, Z. Zhu, H. Zhang, D. Yin, Magnetic dual Z-scheme $g-C_3N_4/BiVO4/CuFe2O4$ heterojunction as an efficient visible-light-driven peroxymonosulfate activator for levofloxacin degradation, Chem. Eng. J. (2022), 139659, https://doi.org/10.1016/j.cej.2022.139659.

[52] D. Awfa, M. Ateia, M. Fujii, C. Yoshimura, Photocatalytic degradation of organic micropollutants: inhibition mechanisms by different fractions of natural organic matter, Water Res. 174 (2020), 115643, https://doi.org/10.1016/j.watres.2020.115643.

[53] H. Huang, X. Han, X. Li, S. Wang, P.K. Chu, Y. Zhang, Fabrication of multiple heterojunctions with tunable visible-light-active photocatalytic reactivity in BiOBr–BiOI full-range composites based on microstructure modulation and band structures, ACS Appl. Mater. Interfaces 7 (1) (2015) 482–492, https://doi.org/10.1021/am5065409.

[54] J. Wu, Y. Xie, Y. Ling, Y. Dong, J. Li, S. Li, J. Zhao, Synthesis of flower-like $g-C_3N_4/BiOBr$ and enhancement of the activity for the degradation of bisphenol A under visible light irradiation, Front. Chem. (2019) 649, https://doi.org/10.3389/fchem.2019.00649.

[55] Y. Sun, W. Zhang, T. Xiong, Z. Zhao, F. Dong, R. Wang, W.-K. Ho, Growth of BiOBr nanosheets on C_3N_4 nanosheets to construct two-dimensional nanojunctions with enhanced photoreactivity for NO removal, J. Colloid Interface Sci. 418 (2014) 317–323, https://doi.org/10.1016/j.jcis.2013.12.037.

[56] S. Cao, B. Shen, T. Tong, J. Fu, J. Yu, 2D/2D heterojunction of ultrathin MXene/$Bi2WO6$ nanosheets for improved photocatalytic CO_2 reduction, Adv. Funct. Mater. 28 (21) (2018), 1800136, https://doi.org/10.1002/adfm.201800136.

[57] X. Yang, W. Liu, C. Han, C. Zhao, H. Tang, Q. Liu, J. Xu, Mechanistic insights into charge carrier dynamics in MoSe2/CdS heterojunctions for boosted photocatalytic hydrogen evolution, Mater. Today Phys. 15 (2020), 100261, https://doi.org/10.1016/j.mtphys.2020.100261.

[58] L. Tan, J. Xu, X. Zhang, Z. Hang, Y. Jia, S. Wang, Synthesis of $g-C_3N_4/CeO_2$ nanocomposites with improved catalytic activity on the thermal decomposition of ammonium perchlorate, Appl. Surf. Sci. 356 (2015) 447–453, https://doi.org/10.1016/j.apsusc.2015.08.078.

[59] J. Zhang, X. Chen, K. Takanabe, K. Maeda, K. Domen, J.D. Epping, X. Fu, M. Antonietti, X. Wang, Synthesis of a carbon nitride structure for visible-light catalysis by copolymerization, Angew. Chem. Int. Ed. 49 (2) (2010) 441–444, https://doi.org/10.1002/anie.200903886.

[60] S. Wei, H. Zhong, H. Wang, Y. Song, C. Jia, M. Anpo, L. Wu, Oxygen vacancy enhanced visible light photocatalytic selective oxidation of benzylamine over ultrathin Pd/BiOCl nanosheets, Appl. Catal. B Environ. 305 (2022), 121032, https://doi.org/10.1016/j.apcatb.2021.121032.

[61] I. Nakamura, N. Negishi, S. Kutsuna, T. Ihara, S. Sugihara, K. Takeuchi, Role of oxygen vacancy in the plasma-treated TiO_2 photocatalyst with visible light activity for NO removal, J. Mol. Catal. A Chem. 161 (1–2) (2000) 205–212, https://doi.org/10.1016/S1381-1169(00)00362-9.

[62] Y. Bu, H. Li, W. Yu, Y. Pan, L. Li, Y. Wang, L. Pu, J. Ding, G. Gao, B. Pan, Peroxydisulfate activation and singlet oxygen generation by oxygen vacancy for degradation of contaminants, Environ. Sci. Technol. 55 (3) (2021) 2110–2120, https://doi.org/10.1021/acs.est.0c07274.

[63] Z. Yang, X. Xia, W. Yang, Y. Liu, Photothermal effect and continuous hot electrons injection synergistically induced molecular oxygen activation for efficient selective oxidation of benzyl alcohol over plasmonic $W_{18}O_{49}/ZnIn_2S_4$ photocatalyst, Appl. Catal. B Environ. 299 (2021), 120675, https://doi.org/10.1016/j.apcatb.2021.120675.

[64] H. Liu, C. Yang, X. Jin, J. Zhong, J. Li, One-pot hydrothermal synthesis of MXene $Ti_3C_2/TiO_2/BiOCl$ ternary heterojunctions with improved separation of photoactivated carries and photocatalytic behavior toward elimination of contaminants, Colloids Surf. A Physicochem. Eng. Asp. 603 (2020), 125239, https://doi.org/10.1016/j.colsurfa.2020.125239.

[65] M. Zuarez-Chamba, S. Rajendran, A. Priya, C. Navas-Cárdenas, Bi-based photocatalysts for bacterial inactivation in water: inactivation mechanisms, challenges, and strategies to improve the photocatalytic activity, Environ. Res. (2022), 112834, https://doi.org/10.1016/j.envres.2022.112834.

[66] P. Kuang, J. Low, B. Cheng, J. Yu, J. Fan, MXene-based photocatalysts, J. Mater. Sci. Technol. 56 (2020) 18–44, https://doi.org/10.1016/j.jmst.2020.02.037.

[67] X. Du, T. Zhao, Z. Xiu, Z. Xing, Z. Li, K. Pan, S. Yang, W. Zhou, $BiVO4@ZnIn_2S_4/Ti_3C_2$ MXene quantum dots assembly all-solid-state direct Z-Scheme photocatalysts for efficient visible-light-driven overall water splitting, Appl. Mater. Today 20 (2020), 100719, https://doi.org/10.1016/j.apmt.2020.100719.

[68] Z. Miao, G. Wang, X. Zhang, X. Dong, Oxygen vacancies modified TiO_2/Ti_3C_2 derived from MXenes for enhanced photocatalytic degradation of organic pollutants: the crucial role of oxygen vacancy to schottky junction, Appl. Surf. Sci. 528 (2020), 146929, https://doi.org/10.1016/j.apsusc.2020.146929.

[69] Z. Chen, H. Yin, R. Wang, Y. Peng, C. You, J. Li, Efficient electron transfer by plasmonic silver in $SrTiO_3$ for low-concentration photocatalytic NO oxidation, Environ. Sci. Technol. 56 (6) (2022) 3604–3612, https://doi.org/10.1021/acs.est.2c00262.

[70] X. Liu, J. Wang, D. Wu, Z. Wang, Y. Li, X. Fan, F. Zhang, G. Zhang, W. Peng, N-doped carbon dots decorated 3D g-C_3N_4 for visible-light driven peroxydisulfate activation: Insights of non-radical route induced by Na^+ doping, Appl. Catal. B Environ. 310 (2022), 121304, https://doi.org/10.1016/j.apcatb.2022.121304.

[71] P. Fageria, R. Nazir, S. Gangopadhyay, H.C. Barshilia, S. Pande, Graphitic-carbon nitride support for the synthesis of shape-dependent ZnO and their application in visible light photocatalysts, RSC Adv. 5 (98) (2015) 80397–80409, https://doi.org/10.1039/C5RA12463H.

[72] Y. Hu, D. Chen, R. Zhang, Y. Ding, Z. Ren, M. Fu, X. Cao, G. Zeng, Singlet oxygen-dominated activation of peroxymonosulfate by passion fruit shell derived biochar for catalytic degradation of tetracycline through a non-radical oxidation pathway, J. Hazard. Mater. 419 (2021), 126495, https://doi.org/10.1016/j.jhazmat.2021.126495.

[73] L. Ren, W. Zhou, B. Sun, H. Li, P. Qiao, Y. Xu, J. Wu, K. Lin, H. Fu, Defects-engineering of magnetic γ-Fe_2O_3 ultrathin nanosheets/mesoporous black TiO_2 hollow sphere heterojunctions for efficient charge separation and the solar-driven photocatalytic mechanism of tetracycline degradation, Appl. Catal. B Environ. 240 (2019) 319–328, https://doi.org/10.1016/j.apcatb.2018.08.033.

[74] H. Li, S. Sun, H. Ji, W. Liu, Z. Shen, Enhanced activation of molecular oxygen and degradation of tetracycline over Cu-S_4 atomic clusters, Appl. Catal. B Environ. 272 (2020), 118966, https://doi.org/10.1016/j.apcatb.2020.118966.

[75] X. He, T. Kai, P. Ding, Heterojunction photocatalysts for degradation of the tetracycline antibiotic: a review, Environ. Chem. Lett. 19 (6) (2021) 4563–4601, https://doi.org/10.1007/s10311-021-01295-8.

[76] Y. Yang, Z. Bian, L. Zhang, H. Wang, $Bi@BiO_x(OH)_y$ modified oxidized g-C_3N_4 photocatalytic removal of tetracycline hydrochloride with highly effective oxygen activation, J. Hazard. Mater. 427 (2022), 127866, https://doi.org/10.1016/j.jhazmat.2021.127866.

[77] Z. Ma, L. Hu, X. Li, L. Deng, G. Fan, Y. He, A novel nano-sized MoS_2 decorated Bi_2O_3 heterojunction with enhanced photocatalytic performance for methylene blue and tetracycline degradation, Ceram. Int. 45 (13) (2019) 15824–15833, https://doi.org/10.1016/j.ceramint.2019.05.085.